



Universiteit
Leiden
The Netherlands

Phase separation in lipid-based nanoparticles: exploring the nano-bio interface

Papadopoulou, P.

Citation

Papadopoulou, P. (2023, November 7). *Phase separation in lipid-based nanoparticles: exploring the nano-bio interface*. Retrieved from <https://hdl.handle.net/1887/3656645>

Version: Publisher's Version

License: [Licence agreement concerning inclusion of doctoral thesis in the Institutional Repository of the University of Leiden](#)

Downloaded from: <https://hdl.handle.net/1887/3656645>

Note: To cite this publication please use the final published version (if applicable).

CHAPTER 3

Lipase-mediated selective hydrolysis of lipid droplets in phase-separated liposomes

This chapter was published as a preprint:

Panagiota Papadopoulou[#], Rianne van der Pol[#], Niek van Hilten[#], Mohammad-Amin Moradi, Maria J. Ferraz, Johannes M.F.G. Aerts, Nico Sommerdijk, H. Jelger Risselada, G.J. Agur Sevink, Alexander Kros* ChemRxiv 2023, DOI: 10.26434/chemrxiv-2023-9q9wh-v3

[#] denotes equal contribution

currently under revision with Advanced Materials

Abstract | The membrane-protein interface in lipid-based nanoparticles is important for their *in vivo* behavior. Better understanding may assist to evolve current drug delivery methods to more precise, cell- or tissue-selective nanomedicine. Previously, we demonstrated how phase separation can drive liposomes to cell specific accumulation *in vivo*, through the selective recognition of phase separation by triglyceride lipases (TGLs). This exemplified how liposome morphology and composition can determine the preferential interaction of nanoparticles with biologically relevant proteins. Here, we investigate in detail the lipase-induced compositional and morphological changes of phase-separated liposomes – which bear a lipid droplet in their bilayer – and unravel how lipase recognizes and binds to the particles at a molecular level. We find that phase-separated liposomes undergo selective lipolytic degradation of their lipid droplet while overall nanoparticle integrity remains intact. Next, we combine MD simulations and *in vitro* experiments to identify the Tryptophan-rich loop of the lipase – a region which is involved endogenously in lipoprotein binding – as the region through which the enzyme binds to the particle. We demonstrate that this preferential binding is due to the lipid packing defects induced on the membrane by phase separation. These findings are a significant example of selective nanoparticle-protein communication and interaction, aspects that may further the control of the *in vivo* behavior of lipid-based nanoparticles.

3.1 Introduction

Lipid-based nanomedicine is undoubtedly a research field of growing importance, with various liposomal drug formulations marketed and used in the clinic over the last decades.¹ More recently, the development of RNA-based lipid nanoparticles (LNPs) has shown great potential, paving the way for future innovations.²⁻⁶ To push this technology forward, towards simpler, yet more efficient and tissue specific formulations for drug delivery, better understanding of nanoparticle behavior must be acquired *i.e.*, how lipid organization determines morphology and influences (desired) nano-bio interactions. A key step is to study the interactions of lipid-based nanoparticles with biologically relevant proteins, and how these are determined by lipid composition and morphology. It is well known that such interactions *i.e.*, lead to the formation of a protein corona which controls the *in vivo* fate of nanoparticles to a great extent;⁷⁻¹⁰ or they can lead to preferential protein binding or induce morphological changes in the membrane and affect the supramolecular assembly,^{11,12} which in turn can affect their *in vivo* fate.

Previously,¹³ in a liposome screening study in zebrafish embryos, a novel liposome formulation (named PAP3) was found to selectively interact with (capillary) lumen-bound triglyceride lipases (TGLs), enzymes involved in lipid transport and metabolism. The interaction led to the selective accumulation of PAP3 liposomes in brain endothelial cells (bECs) of zebrafish embryos which, at this developmental stage, are rich in TGLs. Liposome-lipase interactions are mediated solely through a unique phase-separated lipid nanoparticle morphology, in which liposomes bear a single lipid droplet inside each bilayer (**Figure 1a**). This morphology was found to be the key element for the cell specific accumulation and for interaction with TGLs. This is, to our knowledge, the first time that phase separation is used to target specific cells *in vivo*. PAP3 liposomes consist of an equimolar mixture of 1,2-distearyl-*sn*-glycero-3-phosphatidylcholine (DSPC) – a naturally occurring phospholipid – and 2-hydroxy-3-oleamidopropyl-oleate (DOaG), a synthetic lipid structurally analogous to a diacylglycerol (DAG) (**Figure 1b**). DAGs are endogenous signaling lipids and their conical shape, attributed to the small polar hydroxyl group and bulky fatty acid tails, is associated with negative curvature.

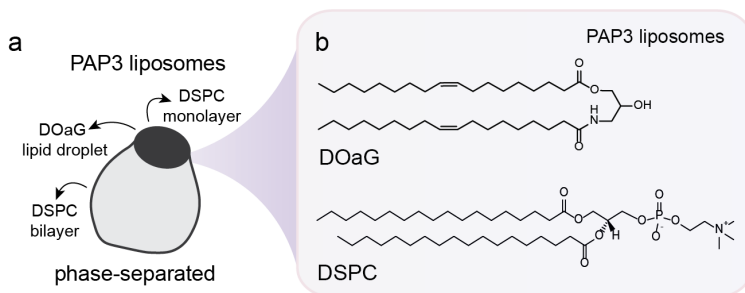


Figure 1. Molecular details of PAP3 liposomes. **a)** Schematic representation of phase-separated liposomes (named PAP3). **b)** Molecular structures of DOaG and DSPC combined in an equimolar mixture (1:1) to form PAP3 liposomes.

Endogenously, their local accumulation in the cell membrane induces morphological changes, which in turn potentiate recruitment and activation of proteins *e.g.*, Protein Kinase C (PKC) or Phospholipase C.^{14–16} When added to phospholipid membranes, they are known to perturb lamellar bilayers and even induce phase separation and formation of non-bilayer phases (*i.e.*, lipid droplets) above a threshold (miscibility) concentration.^{17,18} Our particular liposomal formulation follows the same principles and is an example of how DAG analogues can generate lipid droplets within DSPC leaflets (*i.e.*, lipid droplet is surrounded by a DSPC monolayer). Another important aspect of DAGs is that they increase the spacing between adjacent phospholipid headgroups in a lipid membrane, even below the threshold concentration, an effect that is amplified by curvature.¹⁹ The domains that form as a consequence of such packing frustrations, and transiently expose the apolar domain of the lipid membrane, are known as lipid packing defects.^{18,20–22} Some membrane peripheral proteins have been proposed to rely on these hydrophobic lipid packing defects – caused by factors such as phase separation, lateral tension, or membrane curvature – for membrane binding and activation.^{23,24} Examples include the Golgi-associated protein ArfGAP1, that senses curvature-induced packing defects through an amphipathic lipid packing sensor motif^{25,26} and the CTP:phosphocholine cytidyltransferase (CCT), that binds to large packing defects on lipid droplets.²⁷ Also, the toxin Equinatoxin-II²⁸ and several lipases^{29,30} have been found to sense packing defects induced by DAGs in particular.

Triglyceride lipases (TGLs) are lipolytic enzymes bound at the luminal surface of capillaries, and are involved in lipid transport and metabolism primarily through their interaction with freely circulating lipoproteins. They either hydrolyze tri- and di-acylglycerols and cholesteryl esters or phospholipids, remodeling lipoprotein particles and promoting influx of fatty acids into the cell; or they act as bridging molecules to facilitate lipoprotein uptake.^{31,32} The family consists mainly of hepatic lipase (HL),³³ lipoprotein lipase (LPL),³⁴ and endothelial lipase (EL).³⁵ The main functional domains – the lipid (or lipoprotein) binding domain for substrate binding, the lid region containing the catalytic triad of Serine (Ser), Aspartate (Asp), Histidine (His) and the heparin binding domain – are all structurally homologous throughout the lipase protein family (see^{36,37} and **Figure S24** for protein alignment). The lipid binding domain is rich in hydrophobic residues, mainly tryptophans (Trp), forming a hydrophobic Trp-rich loop that is responsible for insertion of the protein in the hydrophobic lipid core of lipoproteins.^{33,38–41} Importantly, lipases have been found to depend on lipids on the lipoprotein membrane, but not apolipoproteins, for binding.⁴²

Therefore, in this study, we combine experimental characterization and (coarse-grained) molecular dynamics (MD) simulations to investigate the molecular mechanism through which the TGL lipoprotein lipase (LPL) interacts with the DOaG-rich phase separated liposomes, and the subsequent morphological changes of the liposomes upon incubation. First, by combining morphological liposome analysis by cryo-Transmission Electron Microscopy (cryo-TEM) and enzymatic activity analysis of LPL, we observe selective lipolytic degradation of the DOaG-rich lipid droplet of PAP3 liposomes, while the overall nanoparticle integrity and structure is maintained. Mass spectrometry analysis confirms the selective hydrolysis of DOaG over DSPC, consistent with the known preference of LPL for hydrolyzing Tri- and Di-acylglycerols. Next, we built upon earlier insight in the role of defects for protein binding,^{23,24} and study lipid packing defects in PAP3 liposomes and their role in recognition and binding of LPL. By combining cryo-TEM with MD simulations we confirm and quantify increased packing defects on the curved DSPC monolayer surrounding the DOaG lipid droplet, leading to the insight that (induced) curvature and DOaG availability are the two likely ingredients for

selective LPL binding. Finally, free energy calculations and enzymatic activity analysis reveal that the Trp-rich loop of LPL acts as a lipid packing defect sensing motif, that prefers to interact with the defected PAP3 membrane (DSPC/DOaG), over the (flat) pure DSPC counterpart.

3.2 Results

DOaG lipid droplet selectively depleted by lipoprotein lipase

To determine any morphological changes on PAP3 liposomes upon incubation with a TGL, the phase-separated liposomes were incubated with LPL at physiological conditions (pH = 7.4, 37 °C) for 3 h and changes in the morphology were assessed by cryo-TEM imaging (**Figure 2a**). As expected, without addition of LPL nearly 80% of PAP3 liposomes incubating at 37 °C for 3 h were phase-separated (**Figure 2b, e, f** and **Figure S1a**), with only ~20% of the population having another morphology *i.e.*, either (multi-) lamellar, solid-lipid or unidentifiable. Strikingly, after PAP3 liposomes were incubated with LPL they lacked their lipid droplet (**Figure 2c** and **Figure S1b**); less than 10% of the population appeared to be phase-separated (**Figure 2g, h**), and almost 80% of the population were lamellar. This indicated that LPL could deplete the phase-separated droplet possibly through its lipolytic activity, therefore selectively hydrolyzing the DOaG lipid. Accordingly, when the denatured and therefore inactive form of LPL was added to PAP3 liposomes, no change of the phase-separated morphology or the percentage in the population was observed (**Figure 2d, i, j** and **Figure S1c**), implying the catalytically active LPL to be responsible for the selective droplet digestion. Interestingly, despite the major morphological change on PAP3 liposomes, the nanoparticles remained intact in terms of structural integrity, retaining their initial average hydrodynamic diameter of ~120 nm over time, as determined by dynamic light scattering (DLS) (**Figure S2** and **table S1**). Of note, liposomes without DOaG, (*i.e.*, 100% DSPC), did not display any changes in morphology or size before and after addition of LPL (**Figure S3** and **table S1**), suggesting no interaction and as before, signifying LPL to be selective for DOaG or for the phase separation induced by DOaG.

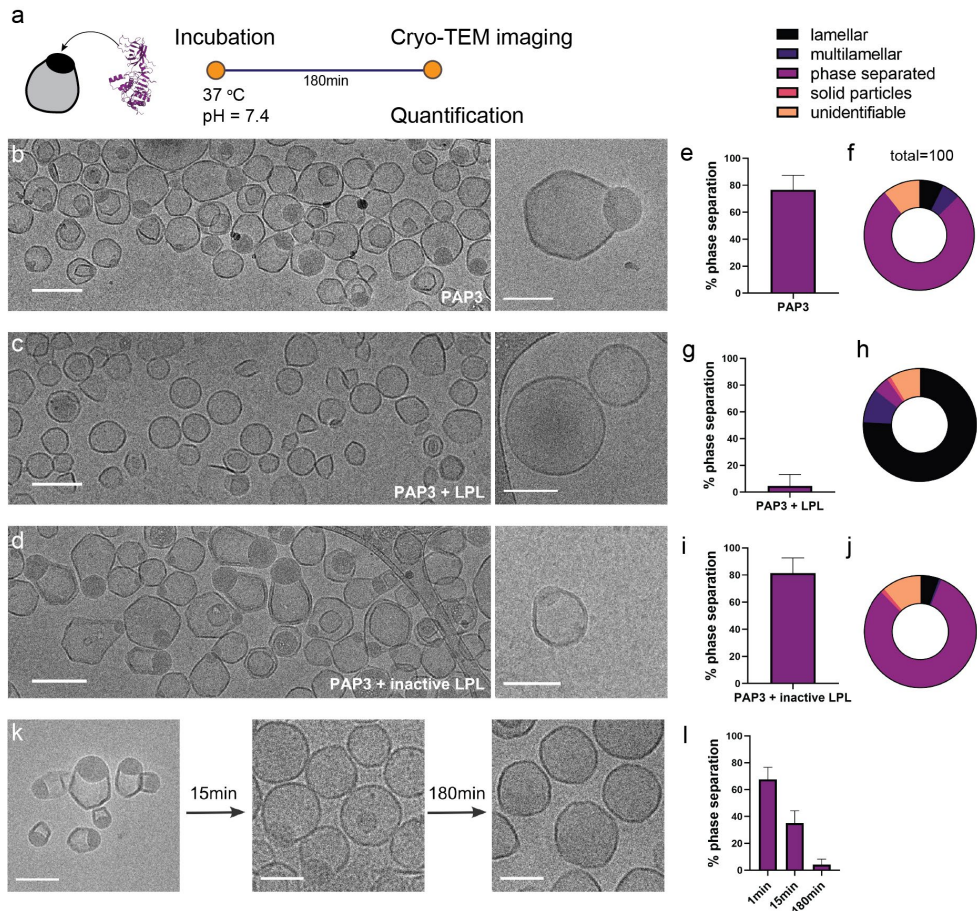


Figure 2. Selective depletion of DOaG lipid droplets in PAP3 liposomes. **a)** Schematic for conditions and timeline of cryo-TEM imaging. Low and high magnification cryo-TEM images depicting PAP3 liposomes incubating at 37 °C for 180 min **b)** without LPL, **c)** with LPL or **d)** with inactive LPL. Percentage of phase separation and quantification, based on cryo-TEM (N=200), of all populations found on PAP3 liposomal formulation incubating at 37 °C for 180 min **e, f)** without LPL, **g, h)** with LPL or **i, j)** with inactive LPL. **k)** Cryo-TEM images of PAP3 liposomes incubating with LPL at 37 °C for 1, 15 and 180 min. **l)** Percentage of phase separation on PAP3 liposomes, based on cryo-TEM quantification (N=200), after incubation with LPL at 37 °C for 1, 15 and 180 min. The data set generated for this figure is a result of the same liposome formulation. Size and PDI values (as determined by DLS) can be found in supporting table S1. Scale bars: 200 nm for b, c, d and 100 nm for k and insets on b, c, d.

LPL selectively hydrolyzes DOaG but not DSPC

Subsequently, to assess the evolution and timeline of the observed morphological change, PAP3 liposomes were imaged after incubating with LPL for 1, 15 and 180 min, and the percentage of phase separation was found to progressively decrease over time (**Figure 2k-l** and **Figure S4**). This indicated the observed phenomenon was a dynamic process, and lipolysis could be monitored over time by quantifying the amount of free fatty acids (FFA),^{43,44} released as metabolite products from the hydrolysis of the co-formulants DOaG and/or DSPC (**Figure 3a**). For this, a non-esterified free fatty acid measurement kit (NEFA-kit) was used, along with mass spectrometry which was used to determine which lipid is preferentially hydrolyzed (**Figure 3b**). As expected, PAP3 liposomes incubated with LPL released ~0.9 mmol/L of FFA over a period of 300 min (**Figure 3c**) and hydrolysis continued beyond this point (**Figure S5**). Incubation of PAP3 liposomes without LPL, or incubation of PAP3 liposomes with inactivated LPL, as well as incubation of 100% DSPC liposomes with LPL, did not release any significant amount of FFA over the same period, again indicating the specificity of LPL for DOaG (**Figure 3c**). Here, to also verify the LPL preference on naturally occurring DAGs – along DOaG as a DAG analogue – we formulated phase-separated liposomes consisting of dioleoylglycerol (DOG) and DSPC (1:1). Subsequently, we monitored the FFA release and structural changes of the DSPC/DOG liposomes upon LPL incubation (**Figure S6**). The results showed similar preference of LPL on DOG-containing liposomes as on PAP3. Similarly, to assess the influence of LPL on liposomes that are known to freely circulate *in vivo* and not particularly interact with cells types and proteins,⁸ a formulation based on the clinically approved Myocet^{®45} (composition: POPC:CHO, 55:45) was also incubated at 37 °C with LPL for 180 min, which did not result in FFA release, indicating no interaction with LPL (**Figure S7**).

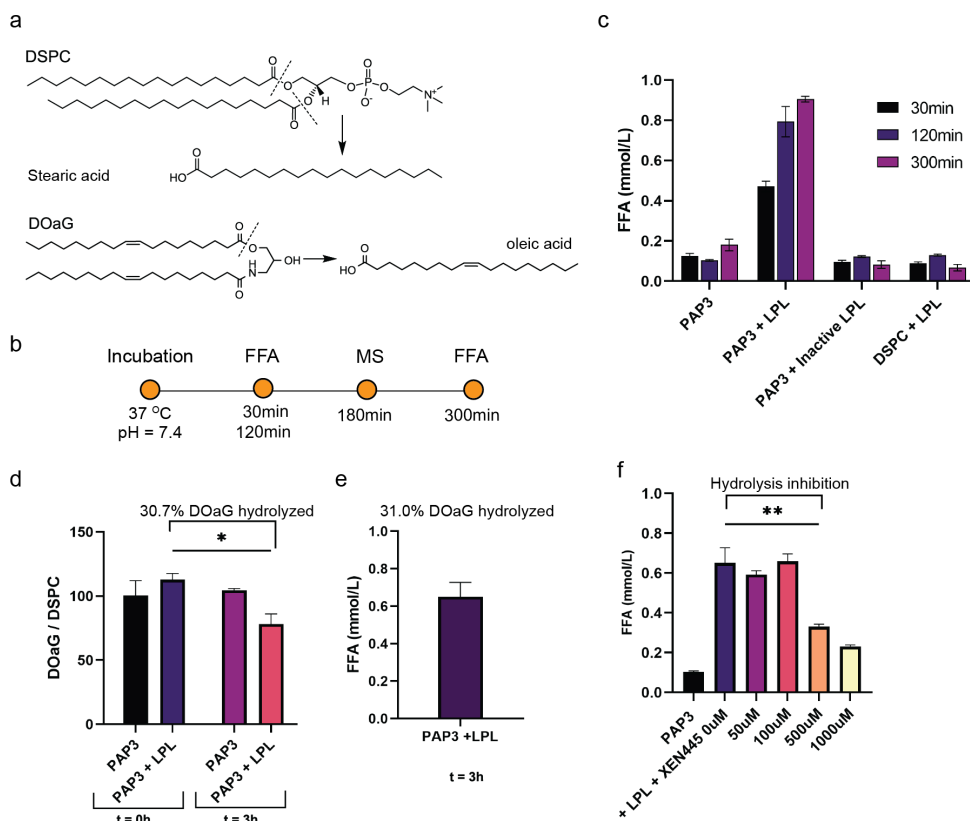


Figure 3. Hydrolysis of lipids in PAP3 liposomes. **a)** Potential hydrolysis of DSPC and/or DOaG co-formulants by LPL resulting in free fatty acid (FFA) release. **b)** Timeline of measurement of LPL hydrolytic activity. **c)** Quantification of released FFA after incubation of PAP3 liposomes without and with LPL, or PAP3 with inactive LPL, or DSPC liposomes with LPL at 37 °C after 30, 120, and 300 min. **d)** Quantification of DOaG / DSPC lipid ratio in PAP3 liposomes as measured by mass spectrometry at $t = 0$ h and $t = 3$ h incubating at 37 °C with and without LPL. DOaG / DSPC ratio of PAP3 at $t = 0$ h was set as 100. Analysis indicated the % of DOaG hydrolyzed. **e)** Quantification of released FFA in PAP3 liposomes incubating with LPL at 37 °C for 3 h, indicating the % of DOaG hydrolyzed. FFA release was measured immediately after the mass spectrometry analysis. The difference on the released FFA of PAP3 between Figure 3c and 3e is attributed to the different concentrations of LPL used for each measurement and therefore hydrolysis must be designated as a range (0.6-0.9 mmol/L). **f)** XEN445-mediated inhibition of LPL and effect on FFA release after PAP3 liposomes incubated with LPL and 0, 50, 100, 500 or 1000 μM XEN445. Size and PDI values (as determined by DLS) can be found in supporting table S1. Statistical significance was evaluated using a two-tailed unpaired Student's t-test. ns: not significant ($P > 0.05$). Significantly different: * $P \leq 0.05$, ** $P \leq 0.01$, *** $P < 0.001$. Exact P value for d : 0.0337 and for f : 0.0020.

Next, mass spectrometry analysis was used to investigate the hydrolysis of the lipids in PAP3 liposomes. The DOaG/DSPC ratio was measured before and after addition of LPL, indicating a decrease only for the DOaG lipid, after addition of LPL, and signifying that 30.7% of DOaG was hydrolyzed (**Figure 3d** and **Figure S8**). Given that DOaG is the only lipid hydrolyzed, FFA was again measured immediately after the mass spectrometry and found to correspond to 31% of hydrolyzed DOaG, in agreement with the mass spectrometry value (**Figure 3e**). In our previous studies,¹³ lipase-mediated uptake of PAP3 liposomes was inhibited *in vivo* (zebrafish embryos and adult mice) by the TGL inhibitor XEN445.⁴⁶ Therefore, we investigated the influence of XEN445 on the lipolytic activity of LPL on PAP3. LPL was incubated with XEN445 at room temperature for 30 min, prior to the addition of LPL to PAP3 liposomes at 37 °C, and DOaG hydrolysis was found to be inhibited by ~50% at 500 μ M XEN445 (**Figure 3f** and **Figure S9**).

Simulations confirm lipase binds on PAP3 liposomes through lipid packing defects and via its Trp-rich lipid binding domain

Having confirmed that LPL selectively hydrolyzes liposomes containing DOaG, we sought to investigate the role of the characteristic phase-separated morphology. Previously, we showed that the concentration of DOaG lipid in the PAP3 formulation determines whether liposomes phase-separate. When PAP3 was formulated with DSPC and 0, 10, or 20% mol DOaG, liposomes did not show phase separation, while above 30% mol DOaG liposomes were found to be phase-separated, causing a directed *in vivo* biodistribution towards TGL-rich endothelial cells.¹³ Therefore, we hypothesized phase separation to be essential – or at least preferable – for TGL recognition. To assess this hypothesis, released FFA after LPL incubation was measured for liposomes with varying % mol of DOaG. Up to 20% mol, *i.e.*, for mixed membranes, FFA release was observed to increase linearly, but it steeply increased after this point (**Figure 4a**). This suggested enhanced LPL action for PAP3 liposomes with $\geq 30\%$ mol DOaG, which coincides with the concentration threshold relating to phase separation as quantified by cryo-TEM (**Figure 4a insets**, **Figure 4b right y-axis** and **Figure S10**). The finding that the phase change coincides with a non-linear jump in the LPL-induced FFA release, signifies the role of phase separation in LPL hydrolysis.

As reported earlier for DAGs,¹⁷⁻¹⁹ increasing the DOaG content in a PC bilayer across a phase boundary, could substantially increase the membrane curvature in the surroundings of the lipid droplet. Curvature is known to notably increase the lipid packing defect number and area, an effect that has been suggested to promote protein binding.^{17,47} Moreover, compared to a mixed membrane, the local concentration of DOaG in the curved membrane around the lipid droplet is also significantly higher. Therefore, to quantify the role of phase separation, curvature, and packing defects at a molecular level – that is not directly accessible by experiments or atomistic MD due to long time scales – we generated a coarse-grained (CG) representation for DSPC/DOaG at different DOaG concentrations (**snapshots** in **Figure 4b** and **Figure S11a**). As detailed in the SI (sections **S12-S15**), the CG DOaG lipid representation was adapted from the similar DOG lipid.⁴⁸ In agreement with standard practice, we employed the observed phase separation onset at 29 % mol (**Figure 4b, left y-axis**) to match the experimental findings. Phase separation in CGMD was quantified by the (time-averaged) relative fraction of contacts between the DOaG lipid and the DSPC lipid (see Materials and Methods for more details and **Figure S14**) following a recently developed method.⁴⁹ The DOaG parametrization described here was used for all simulations in the remainder of this study.

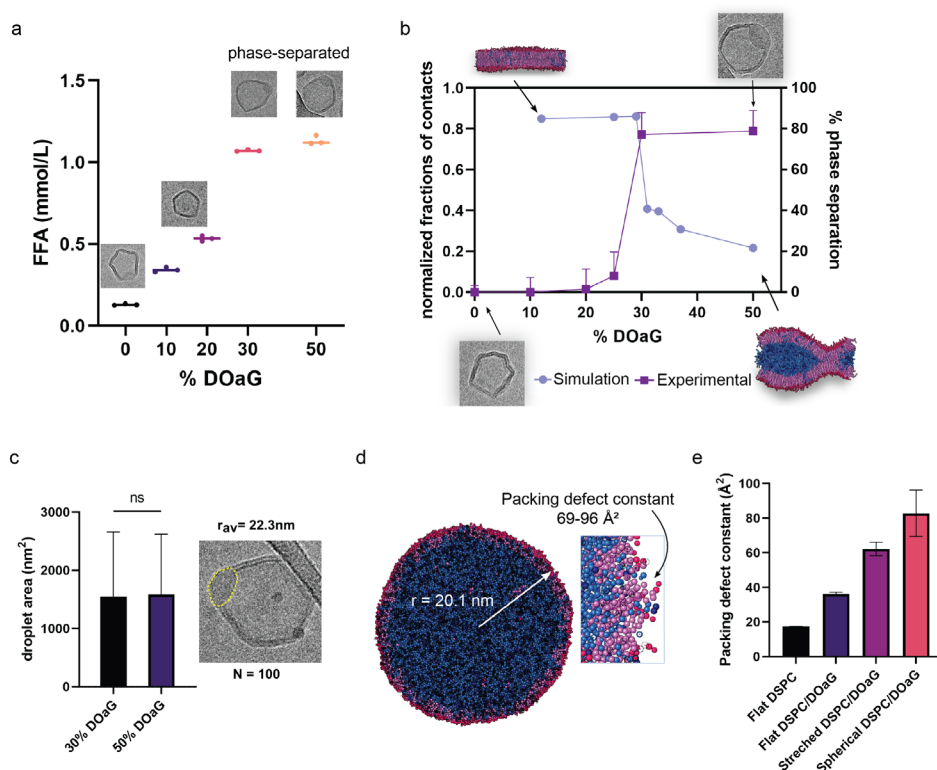


Figure 4. Experimental findings and simulations confirm phase separation as an important aspect for LPL preferential binding on PAP3 liposomes **a)** Quantification of released FFA of formulations containing DSPC and varying % mol of DOaG, after incubation with LPL at 37 °C for 120 min. Insets show the morphology of liposomes at a particular % mol DOaG (0% = gel phase, 20% = small droplet indicate initiation of phase separation, 30-50% = phase-separated). **b)** Double plot showing correlation of experimental and simulation data. Phase separation starts after 25% mol DOaG according to cryo-TEM quantification (N=200) and 29% according to the coarse-grained simulation. DOaG is shown in blue and DSPC is shown in pink/red. **Correlation of simulated PAP3 droplet and experimental values.** **c)** Average radius of phase-separated PAP3 liposomes (containing 30% or 50% mol DOaG) as calculated by cryo-TEM quantification of the droplet area (N=100). Area was measured in Fiji software, by drawing the perimetry of each droplet (yellow dashed line) according to the electron density. **d)** Simulated PAP3 spherical droplet with radius approximately matching the experimental value in (c) and zoom-in inset depicting the lipid packing defects. Packing defect constant determined as the effective average area of hydrophobic defects and calculated to be 69-96 Å² for the spherical droplet. DOaG is shown in blue and DSPC is shown in pink/red. **e)** Packing defect constants of flat DSPC, flat DSPC/DOaG, stretched DSPC/DOaG and spherical DSPC/DOaG (see d). Size and PDI values (as determined by DLS) can be found in supporting table S1. Statistical

significance was evaluated using a two-tailed unpaired Student's t-test. ns: not significant ($P > 0.05$). Significantly different: * $P \leq 0.05$, ** $P \leq 0.01$, *** $P < 0.001$. Exact P value for c: 0.8152, e: 0.0002 and < 0.0001 . For graphs in b, lines were drawn for the clear visualization of the phase separation point.

To capture the role of curvature and to quantify the defect characteristics for a DOaG droplet of a typical diameter of – *i.e.*, an average of 22.3 nm for ≥ 30 % mol DOaG (see **Figure 4c**) as quantified by cryo-TEM – we performed a droplet simulation with this initial radius for a 82/18 DOaG/DSPC ratio (**Figure 4d** and **Figure S11b**). Since demixing is strongly diffusion limited, we started from a pre-structured droplet and performed 2 microsecond of simulated annealing, to quickly reach a stable structure, with the droplet radius stabilizing to 20.1 nm. Using a modified protocol (see Materials and Methods), we calculated the packing defect constant, which is a measure of the effective average area of hydrophobic defects (**Figure 4d, e** and **Figure S16**). For a flat DSPC membrane the constant was found to be $\sim 17 \text{ \AA}^2$ while adding the DOaG to the system (1:1 ratio) increased the constant to $\sim 36 \text{ \AA}^2$ indicating phase separation increases the packing defects. Also, adding curvature increased the packing defect constant even further – as calculated by the defect constant on the curved droplet (**Figure 4d, e**). For the latter, however, we give a range since the lipid composition in the droplet monolayer varies, depending on the starting configuration and size, and because there is an uncertainty in the fitting parameter. The range for the packing defect constant was between 69 to 96 \AA^2 , showing that the packing defects in the curved droplet are more prevalent than in the flat pure DSPC and flat DSPC/DOaG membranes (**Figure 4d zoom in, and Figure 4e**). We next used the lower bound of this value range as a reference value for simulating LPL binding to stretched DOaG/DSPC membranes (**Figure 4e and 5c**). Stretched membranes are used to approximate curved membranes, since the lipid packing defects on their outer leaflet surface correlate, as we explain in reference⁵⁰ (*vide infra*).

Following the proof that the DOaG droplet increases both the number and area of lipid packing defects in the curved DSPC monolayer – due to the condensing of DOaG and the accompanying high curvature of the outer leaflet – we next sought to investigate whether LPL specifically binds to PAP3 via these packing defects. The structure of LPL is well studied and identified by X-ray crystallography⁵¹ and cryo-TEM⁵² (**Figure 5a**). Functional parts include the lipid binding domain which is rich in Trp as mentioned previously (hence called the Trp-rich loop, **Figure 5a, inset**), and the catalytic lid with the active site (**Figure 5a, inset**). The C-terminus, where the lipid binding domain is located, is responsible for substrate binding but not for heparin binding or catalysis.⁵³ We first proceeded to investigate which regions of the LPL protein may be involved in interacting with the lipid packing defects of the phase-separated membrane. Hereto, we employed a recently developed neural network (NN) model that is trained on MD data and is able to predict the lipid packing defect sensing free energy ($\Delta\Delta F$) for peptide sequences.⁵⁴ $\Delta\Delta F$ is defined as the difference in free energy of a peptide binding to a tensionless membrane versus a stretched membrane that bares lipid packing defects, such as the curved DSPC monolayer around a DOaG droplet. The higher the magnitude of the $\Delta\Delta F$ value, the more favorably it binds to the defected membrane. We first used a sliding window of 15 residues to fragmentize the LPL protein structure and then predicted the $\Delta\Delta F$ for the overlapping fragments. From this, we derived a per-residue average $\Delta\Delta F$ (given the residue is solvent accessible, see section **S17** and **Figure S18**) and color-coded the protein structure accordingly (**Figure 5b**).

Residues Ser416-Ser426, comprising the Trp-rich loop, was the highest scoring solvent-accessible peptide motif we identified (**Figure 5b** and section **S19**). As previously described in the context of membrane curvature sensing, Trp residues can indeed play a key role in complementing the hydrophobic lipid packing defects on lipid leaflets,²⁵ and we argue that the Trp-rich loop of LPL might fulfill a similar function. Notably, this argument is in line with the Trp-rich loop being part of the lipid binding domain of LPL, which is responsible for endogenous lipoprotein binding.^{38–40}

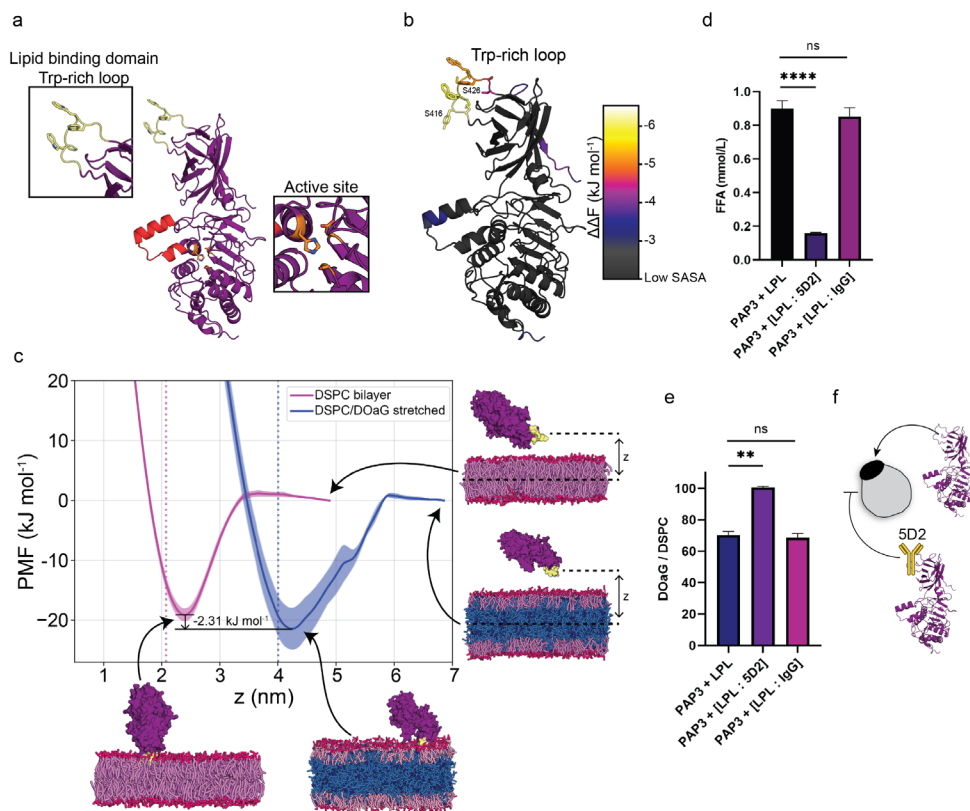


Figure 5. LPL binds to PAP3 liposomes via its Trp-loop. **a)** Structure of LPL (*Bos Taurus*). Insets indicate the Trp-rich loop (yellow) – which comprises the lipid binding domain – and active site (orange). Lid region indicated in red. **b)** Color-map of predicted lipid packing defect sensing regions on LPL (all values are given in S19). Bright colors indicate putative sensing motifs, according to NN-predicted relative binding free energy ($\Delta\Delta F$) and solvent-accessible surface area (SASA) values. **c)** Potential of mean force (PMF) profiles of LPL binding to a DSPC membrane (in red-pink) and a DSPC/DOaG phase-separated membrane (in red-pink/blue). The umbrella sampling (US) reaction coordinate is the z -distance between the center-of-mass (COM) of the Trp-rich loop (in yellow) and the COM of the lipids (*i.e.*, center plane of the membrane). Snapshots are the final frames of the trajectories and indicate that the protein is completely unbound at high z (free energy = 0 kJ mol⁻¹) and membrane-bound through the Trp-rich loop at the minima. Dotted lines indicate the position of the DSPC head groups (NC3 beads). **d)** Quantification of released FFA from PAP3 liposomes and **e)** mass spectrometry quantification of DOaG / DSPC ratio of PAP3 liposomes after incubation at 37 °C for 120 min with LPL, LPL + 5D2 antibody and LPL + IgG control antibody. DOaG/DSPC ratio of liposomes that did not undergo hydrolysis incubating with LPL + 5D2 was set as 100. **f)** Schematic of LPL binding to PAP3 liposomes via its Trp-rich loop and 5D2 mediated inhibition of binding. Size and PDI values (as determined by DLS) can be found in supporting table S1. Statistical significance was

evaluated using a two-tailed unpaired Student's t-test. ns: not significant ($P > 0.05$). Significantly different: $*P \leq 0.05$, $**P \leq 0.01$, $***P < 0.001$. Exact P value for d: <0.0001 and 0.3222 and for e: 0.0029 and 0.5654 .

To further investigate lipid packing defect sensing by LPL and to see whether the Trp-loop is preferably binding to defected membranes such as the PAP3 liposomes, we calculated the potential of mean force (PMF) profiles for the entire LPL protein binding to the PAP3 phase-separated membrane – with lipid packing defect constants that are in a similar range as those for the earlier simulated PAP3 droplet (*vide supra*, **Figure 4e**). We performed umbrella sampling (US) simulations with the z-distance between the Trp-rich loop and the center plane of the membrane as the reaction coordinate. The resulting PMF profiles showed that LPL binds to the PAP3 phase-separated membrane (having enhanced lipid packing defects) indeed more favorably than to a flat pure DSPC bilayer, with a small free energy difference of 2.31 kJ mol^{-1} ($\sim 1 \text{ k}_B\text{T}$) between the minima (**Figure 5c**). The propensity for binding that is observed for the flat pure DSPC membrane (about 20 kJ mol^{-1}) corresponds exactly to the curvature sensing transition point from a recent study,⁵⁴ which showed that a 2 kJ mol^{-1} increase in binding free energy has a pronounced effect on the membrane binding probability (**Figure S20**).

Moreover, although a conformational change in the binding domain may contribute a few kJ mol^{-1} to the actual binding affinity,⁵⁵ this shift is likely very similar for both membranes. Beyond this binding preference, the enzymatic preference of LPL to hydrolyze DAGs over phospholipids⁵⁶ *is not* captured by our MD simulations but *does* contribute to our experimental observations. From the MD trajectories, it is clear that LPL indeed interacts with the membranes through its Trp-rich loop (**snapshots** in **Figure 5c**), in line with the NN-predictions (**Figure 5b**), and mechanistically similar to previously reported lipid droplet sensing proteins.^{57,58}

To experimentally prove the involvement of the Trp-rich loop in the recognition and hydrolysis of PAP3 liposomes, we measured the hydrolytic activity of LPL on PAP3 liposomes, while blocking the Trp-rich loop with the monoclonal anti-LPL antibody 5D2. The 5D2 monoclonal antibody has been identified to bind specifically

to the Trp-loop of the lipid binding domain of LPL, inhibiting binding and catalysis of lipoproteins.^{40,59–61} Indeed, after incubation of LPL with 5D2 in a 1:1 ratio at room temperature for 30 min and subsequent addition to PAP3 liposomes at 37 °C, hydrolysis of DOaG as quantified by the release of FFA and mass spectrometry was strongly reduced (**Figure 5d-f**). To ensure that inhibition of hydrolysis was due to the specific inhibition of the Trp-rich loop by the 5D2 antibody, a negative isotype control antibody (matching 5D2 antibody's host species and class - IgG1) was used to measure the non-specific binding in LPL and non-specific interactions with PAP3. As expected, the control antibody did not inhibit the hydrolysis (**Figure 5d, e**), supporting the specific interaction of LPL with PAP3 liposomes through its Trp-rich loop. Similarly, when a non-mammalian LPL (derived from *Burkholderia sp.*) – which lacks the lipid binding domain of mammalian TGLs – was used with the 5D2 antibody (**Figure S21** for complete sequence), hydrolysis was not inhibited (**Figure S22**), indicating again the specificity of 5D2 to the Trp-rich loop. Despite the hydrolysis of PAP3 liposomes taking place with the non-mammalian lipase, it appears to occur via a different mechanism, and it is therefore not relevant for the study of mammalian LPL species. It *does* however signify that 5D2 inhibits the Trp-loop specifically, and non-specific interactions between antibody-protein-liposomes do not take place.

3.3 Discussion and Conclusion

In this work, we combine experimental findings and MD simulation data to describe the selective lipolytic degradation of lipid droplets in phase-separated liposomes by LPL. We show LPL recognizes the enhanced lipid packing defects on the liposomal membrane induced by phase separation. The liposomes, named PAP3, consist of the naturally occurring DPSC and the synthetic DAG analogue DOaG, in a 1:1 ratio, with the latter being responsible for the phase separation and constitution of a lipid droplet within each liposome bilayer. PAP3 liposomes have been seen to interact with TGLs and specifically accumulate in cell subsets *in vivo*,¹³ a phenomenon attributed to their phase-separated morphology. Therefore, the observation of their structural evolution after interaction with LPL, as well as the mechanism of enzyme

binding was of great interest. Here, we confirm the selective hydrolysis of DOaG by LPL, leading to degradation of the lipid droplet and to reorganization of the assembly to a lamellar bilayer, while the overall integrity of the nanoparticle is maintained. Contrarily, the other co-formulant – DSPC – does not undergo hydrolysis. These observations exemplify selective nanoparticle-protein interactions and subsequent nanoparticle rearrangement. As TGLs endogenously remodel lipoproteins without nanoparticle collapse – *i.e.*, LPL remodels very low-density lipoproteins to low-density lipoproteins^{34,62,63} – here we similarly show the depletion of a large part of the nanoparticle without bilayer disruption.

Additionally, we show that LPL is selective for PAP3 liposomes (DSPC/DOaG) and for liposomes containing the natural DAG counterpart (DSPC/DOG). LPL is not selective for 100% DSPC liposomes, or typical spherical LUVs with high circulation lifetimes *in vivo* (*i.e.*, Myocet[®]-like). One reason for this could be the inherent preference of LPL to hydrolyze DAGs and therefore DAG analogues, such as DOaG. Synergistically, another reason could be the preference of LPL to recognize membranes with high curvature – and thus higher packing defect constants – induced by phase separation.^{15,16,24} This hypothesis is supported by the non-linear increased hydrolysis on liposomes consisting of $\geq 30\%$ mol DOaG (phase-separated), over liposomes consisting of $< 25\%$ mol DOaG (non-phase separated). Lipid packing defects were then quantified in our coarse-grained MD simulations and found to be higher when phase separation and high curvature are present in the membrane system. Finally, we show that LPL preferentially binds to the defected membrane of PAP3 liposomes, and we identified the Trp-rich loop of LPL as a lipid packing defect sensing motif. Preventing the Trp-loop to bind to PAP3 (by blocking the region with the selective antibody 5D2)⁵⁹, abolishes the lipolysis and confirms the involvement of the Trp-rich loop in the recognition of PAP3 liposomes. Hereby, we expand our knowledge of the Trp-rich loop to act as a lipid packing defect sensor, beyond its role in lipoprotein binding.³⁸ PAP3 liposomes, having lipid packing defects that arise upon phase separation, appear to hijack the natural pathway in which LPL recognizes lipoproteins via its Trp-rich loop.

Additionally, we have previously shown PAP3 liposomes to be endocytosed by a TGL-mediated pathway *in vivo*.¹³ A possible pathway for this could be the selective recognition of DOaG by TGL – with a significantly higher chance of DOaG being transiently exposed to the aqueous environment due to the increased packing defects in the phase-separated membrane – and subsequent endocytosis. Our current study shows the selective lipolysis and remodeling of the particle by LPL, something that may also occur *in vivo* before nanoparticle uptake by the cell. However, given the complex *in vivo* environment and the spatiotemporal regulation of lipase function in lipid metabolism, further studies should be performed *in vivo* and in real time to solidly prove this hypothesis. Here it should be noted, apolipoprotein CII (APOCII) is an essential co-factor of LPL and, in a physiological environment, it will play a central role on efficient lipase activity.³⁴ This is an aspect that is not presented in the current study. However, the presence of apolipoproteins is not vital for LPL binding on lipid membranes⁴² and, although APOCII would enhance the LPL lipolytic efficiency (or would even be essential in an *in vivo* environment), it is not required for overall LPL activity; especially not for comparison of relative activity on different targets (*i.e.*, different liposomal formulations).

In the case of *in vivo* selective lipolysis of the PAP3 lipid droplet – without nanoparticle collapse as this study suggests – these nanoparticles can exert unique properties for drug delivery *i.e.*, the lipid droplet could be used as a guide “moiety” for cell selective accumulation through a lipase-mediated pathway, while the hydrophilic core could incorporate functional drugs. Alternatively, pro-drugs could be incorporated within the lipid droplet exploiting the selective lipase interaction for specific drug release *i.e.*, lipase-mediated prodrug hydrolysis and subsequent drug release. However, the most important aspect of this work is not to address potential drug-delivery designs, but to overall understand in detail how interactions with the biological environment influences lipid-based nanoparticle properties. Ultimately this will lead to more rational drug-delivery designs. Another noteworthy observation is the visible remnants of the hydrolyzed droplet on some nanoparticles (**Figure S23, arrows**). Such thickness mismatches in cryo-TEM have been recently described as nanodomains in liposomal membranes.^{64,65} Therefore,

although PAP3 liposomes can be seen as lamellar and non-phase separated macromolecularly after LPL incubation, a more in-depth investigation of the molecular details is required – *e.g.*, the existence of nanodomains or lipid rafts remaining after LPL hydrolysis. The question that arises here is whether such nanodomains can be still recognizable by TGLs *in vivo*.

Finally, the selection of LPL as a representative TGL was purely due to the extensive literature on LPL structure, regulation and function in health and disease, and therefore was the most relevant protein to base our studies on. However, all (mammalian) lipases from the TGL family have very similar amino acid sequences (³⁶ and **Figure S24** for protein alignment), structural homology, and similar functional roles on triglyceride metabolism.^{33,66–68} This allows the assumption that other TGLs will behave similarly on PAP3 liposomes as the LPL studied here. On the same note, the LPL chosen for these studies was derived from bovine milk (*Bos Taurus*), yet the sequence homology with human LPL (*Homo Sapiens*) is > 90%, with high structural similarity and a conserved Trp-loop (see **Figure S25-S26** for protein structure alignment), which allows to assume that it will similarly affect PAP3 liposomes as bovine LPL. To support this, we show that incubating PAP3 liposomes with human LPL releases a substantial amount of FFA (**Figure S27**). Also, similar PMF profiles were calculated for human LPL interacting with the DOaG/DSPC phase-separated membrane and a flat DSPC bilayer through its Trp-rich loop, showing even a more substantial binding preference for the phase-separated system in terms of the free energy difference between the minima (13.48 kJ mol⁻¹) (**Figure S28**).

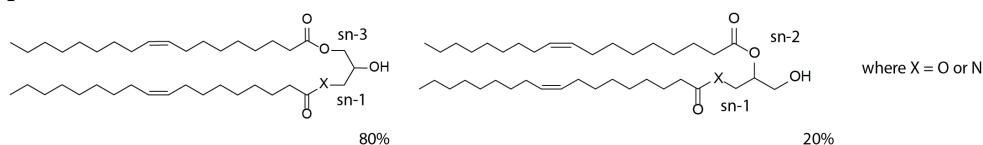
Overall, this study explains in detail the how and the why of the preferential interaction of TGLs with unique phase-separated liposomes. Such interaction has been recently found responsible for cell specific targeting *in vivo*. Particularly, it serves an important proof-of-concept for selective protein interaction on lipid nanoparticle membranes, owing to lipid packing defects. Comparable to the formulation studied here, some RNA-based lipid nanoparticles (RNA-LNPs) have membranes with high curvature. They consist of a solid lipid core, surrounded by a phospholipid monolayer and – depending on composition – they may be prone to such packing defects. Therefore, this study could open new avenues for exploration

of novel LNP formulations, that could preferentially interact with packing-defect sensing motifs in proteins of interest. Most notably, this work presents a selective lipid-based nanoparticle - protein communication and emphasizes the morphological changes nanoparticles undergo after interaction with physiologically relevant proteins. Persistent and limited understanding of the key nano-bio interactions has so far stymied progression from empirical discovery towards rational nanoparticle design. Therefore, understanding the nanoparticle - protein interface is an aspect that could lead to more advanced and precise nanomedicines in the future.

3.4 Materials and Methods

General reagents: 1,2-distearoyl-*sn*-glycero-3-phosphatidylcholine (DSPC) was purchased from Avanti Polar Lipids (Alabaster, AL, US). Additional DSPC was purchased from Lipoid GmbH. XEN445, Lipoprotein Lipase derived from Bovine milk and Lipoprotein Lipase derived from *Burkholderia Sp.* was purchased from Sigma Aldrich. Human LPL (recombinant derived from CHO cells) was purchased from R&D systems, Bio-technie. Non-Esterified Fatty Acid measurement kit (NEFA-HR2, FUJIFILM Wako chemicals) was purchased from Sopachem, the Netherlands. Anti-lipoprotein lipase monoclonal antibody – 5D2 clone and negative IgG isotype control – was purchased from Biorad, United Kingdom. All other chemical reagents were purchased at the highest grade available from Sigma Aldrich and used without further purification. All solvents were purchased from Biosolve Ltd. Ultrapure MilliQ® water, purified by a MilliQ Advantage A10 water purification system from Millipore, was used throughout.

Synthesis of DOaG and DOG lipids: DOaG and DOG lipids were synthesized as previously reported (chapter 2 and reference ¹³) and isolated as regioisomeric mixtures: 80% isomer where acyl chains substituting the *sn*-1 and *sn*-3 positions of the backbone and 20% isomer where acyl chains substituting the *sn*-1 and *sn*-2 positions of the backbone):



Lipoprotein Lipase: Lipoprotein Lipase (from bovine milk) in ammonium sulfate suspension was centrifuged in a low protein binding tube (DNA Lobind, Eppendorf) for 15 min at 15.000 g (at 4 °C) and the supernatant was removed. The precipitate was then dissolved gently in Tris Buffer 10mM, pH 7.4 and spun again for 15 min at 15000 g. The supernatant containing the dissolved protein was then kept and concentrated with spin filtration (Amicon, MWCO 10 kDa). The new concentration was determined using a NanoDrop™ One/One^C Microvolume UV-Vis Spectrophotometer (Thermo Scientific) according to Lambert's beer equation ($A = \epsilon b c$) with an extinction coefficient $\epsilon = 71040$ L/mol.

To ensure retrieval of all LPL from the manufacturer's bottle, any leftover precipitate in the bottle was dissolved in Tris Buffer (10 mM, pH = 7.4) and dialyzed against the same buffer to remove residual ammonium sulfate (dialysis cassettes, Slide-A-Lyzer™, 20K MWCO, ThermoFisher Scientific). The solution was then centrifuged at 15000 g for 15 min and the supernatant was kept, concentrated and concentration was determined as stated above. LPL was then aliquoted in low protein binding tubes (DNA Lobind, Eppendorf) and kept at -80 °C until usage. Lipoprotein Lipase in PBS (Human, derived from CHO cells) was firstly dialyzed against Tris Buffer 10 mM pH = 7.4 and then concentrated. The new concentration was determined as described above. Similarly, it was kept at -80 °C aliquoted for further use.

Liposome formulation: Large unilamellar vesicles (LUVs) were formed through extrusion (mini extruder, Avanti Polar Lipids) above the T_m of all lipids (*i.e.*, 65-70 °C) in 10mM Tris Buffer pH = 7.4 and at a total lipid concentration of 5 mM (3.5 mg/mL), unless if stated otherwise. Individual lipids as stock solutions (10 mM) in chloroform, were combined to the desired molar ratios and dried to a thin film, first under N₂ stream, then >1 h under vacuum. Lipid films were hydrated with 1 mL Tris Buffer above the T_m of all lipids (65-70 °C), with gentle vortexing, to form a suspension. Hydrated lipids were passed 11 times through 2 x 400 nm polycarbonate (PC) membranes (Nucleopore Track-Etch membranes, Whatman), followed by 11 times through 2 x 100 nm PC membranes. All liposomes were stored at 4 °C and used within 5 days.

Liposome - Lipase Incubation: Liposomes (3.5 mg/mL, in 10mM Tris Buffer, pH = 7.4) were transferred in a low protein binding tube (3 mg/mL final lipid concentration after lipase incubation) and subsequently Lipoprotein Lipase (in

10mM Tris Buffer pH = 7.4) was added to the tube to reach 0.03 mg/mL final concentration. Liposome-lipase mixture was left to incubate at 37 °C in a thermomixer (Eppendorf) for up to 20 h with gentle occasional mixing.

Inactivation of LPL: Lipase in Tris Buffer (10mM, pH=7.4) was added in a low protein binding tube (DNA LoBind, Eppendorf) and heated up to 95 °C for 10 min in a thermomixer (Eppendorf) to ensure denaturation.

Inhibition of LPL by XEN445 inhibitor: To inhibit the catalytic activity of LPL before incubation with PAP3 liposomes, the lipase was incubated for 30 min at room temperature with the TGL inhibitor XEN445 at different concentrations (titration). The inhibitor was freshly dissolved in DMSO as a stock solution of 10 mM and subsequently added to a low-protein binding Eppendorf tube (DNA-LoBind) containing LPL, to reach final concentration of 0, 50, 100, 500 or 1000 μ M and at a constant DMSO content of 5% v/v. LPL concentration was so that it would reach 0.03 mg/mL final concentration after incubation with liposomes, as stated previously.

Size and polydispersity measurements: Particle size and polydispersity were measured using a Malvern Zetasizer Nano ZS (operating wavelength = 633 nm). Measurements were carried out at room temperature (25 °C) or at 37 °C in Tris Buffer 10 mM, pH = 7.4 and at a total lipid concentration of approx. 100 μ M. All reported DLS measurements are the average of three measurements.

FFA release measurement: For each time point of interest, the amount of FFA released in the sample was measured with a non-esterified fatty acid assay kit (NEFA kit – Fujifilm Wako Chemicals) with a protocol provided for 96 well plates (Greiner) using a microplate spectrophotometer set to 37 °C (Infinite®, M1000 pro, TECAN). Briefly and for each sample, 9 μ L were taken and diluted 2x in Tris Buffer 10 mM (pH = 7.4). 5 μ L were then put in each well and mixed with 200 μ L of Reagent 1 and incubated for 5 min. The absorbance (Abs1) was then measured in each well at 550 nm (Sub: 660 nm). Immediately after, 100 μ L of Reagent 2 was added and the mixture was incubated for another 5 min. The absorbance (Abs2) was again then measured in each well at 550 nm (Sub: 660 nm). Final absorbance was calculated by subtracting Abs1 from Abs2. Concentration of FFA (mmol/L) was calculated by constructing each time a new calibration curve. All measurements were the average of three measurements.

Cryogenic Transmission Electron Microscopy: Freshly glow-discharged carbon grids supported on Cu (Lacey carbon film, 200 mesh, Electron Microscopy Sciences, Aurion, The Netherlands) were used for vitrification inside a Vitrobot plunge-freezer (FEI VitrobotTM Mark III, Thermo Fisher Scientific) regulating steady temperature and humidity conditions (22 °C or 37 °C and 99% humidity). Liposomes incubating with LPL at 37 °C were immediately taken and applied to the grid and the excess liquid was blotted for 3 s and subsequently plunge frozen in liquid ethane below -160 °C to ensure formation of vitreous ice. cryo-TEM images were collected on a Talos L120C (NeCEN, Leiden University) operating at 120 kV or on a Titan (TU Eindhoven) operating at 300 kV, with working temperature below -180 °C. Images were recorded manually at a nominal magnification of 13500x, 22000x or 36000x yielding a pixel size at the specimen of 7.41, 4.44, or 2.86 ångström (Å), respectively.

Cryo-TEM Quantification: Software Fiji (ImageJ) was used for image processing and quantification. Individual low magnification images (up to 3 images per sample) were used to provide a big population of 200 nanoparticles. Particles were then counted and divided into categories (lamellar, multilamellar, phase-separated, solid particles), according to their morphology. Liposomes whose morphology was not able to be identified (due to image quality) were marked as “unidentifiable” and the value obtained was used as standard deviation for the rest of population. Liposomes that were seen to be on top or in close contact with the copper grid or overlapping with each other, were excluded from the quantification. Particles consisting of two distinct liposomal cores and one lipid droplet (*i.e.*, sharing the droplet) were quantified as one phase-separated particle. For quantification and calculation of the radius of the PAP3 droplet, the area A (nm²) of each individual droplet ($N = 100$) was measured by the 2D projection of liposomes as obtained by cryo-TEM imaging. The average droplet radius r (nm) was then calculated from the formula: $A = \pi r^2$.

Simulation details: All simulations were performed with GROMACS 2019.3⁶⁹ and the Martini 3.0.0 force field,⁴⁸ at a 20-fs time step. Temperature ($T = 303.15$ K, $\tau_T = 1$ ns) and pressure coupling (compressibility = $4.5 \cdot 10^{-5}$ bar⁻¹, $\tau_p = 12$ ns) were applied by the velocity rescaling thermostat and the Berendsen barostat, respectively. The neighbor list was updated every 20 steps. A 1.1 nm cutoff was used for the Van der Waals interactions (shifted Verlet cutoff scheme) and Coulomb interactions (reaction-field electrostatics).

Coarse-grained model for PAP3 liposomes: Phase separation on PAP3 liposomes was determined from the MD trajectories, using the time-averaged contact fraction between the DOaG and the DSPC lipid. Following a general procedure,⁴⁹ a relative contact fraction was calculated by counting contacts between DOaG and DSPC lipids and dividing it by the total number of DOaG contacts (see sections **S12-S15** for details). A cutoff of 1.1 nm was used to identify contacts between lipids via selected beads on both lipid types that are roughly at the same depth within the membrane. In addition, we normalized by the total concentration of DOaG to enable direct comparison for different DOaG concentrations. Consequently, complete phase separation always corresponds to a value of zero, and ideal mixing to unity.

Droplet simulation: For the simulation of the droplet, the droplet configuration was made with PackMol⁷⁰ with - on the inside - purely DOaG and on the outside a monolayer of DSPC. The simulated annealing was run for 1.5 μ s, with a starting temperature of 450 K and cooled to a temperature of 303 K, after which the temperature was kept stable for 500 ns at the final temperature. After the simulated annealing the droplet was ran for analysis for 1.5 μ s at the same temperature and settings as the bilayer simulations.

Packing defects: While previous work used the PackMem package⁷¹ to identify a linearly increasing defect size constant with total curvature for both single component and mixed membranes,¹⁹ the role of (de)mixing remains less quantified. Here, we developed a new computational protocol to clarify this relation for our highly curved DOaG/DSPC membranes of arbitrary (non-symmetric) shapes. Packing defect constants for the simulated PAP3 droplet can in principle be determined using standard PackMem routines, by employing a spherical instead of the usual rectangular grid.¹⁹ However, since droplets do not necessarily adopt a

purely spherical shape, even tiny mismatches in the determination of the relevant reference interface may bias the calculated constants in a non-predictable fashion. For this reason, we developed a protocol that can deal with arbitrary shapes. Briefly, a closed 2D interface is fitted through the positions of relevant GL beads, subsequently triangulated, and used as a reference for identifying shallow and deep defects following the recommended PackMem settings.⁷¹ Details and examples of this procedure will be published in a separate study.

Protein modeling and lipid packing defect sensing prediction: The 3D models of human and bovine LPL were downloaded from the AlphaFold2 database.^{72,73} Both structures closely overlap with the human crystal structure⁵¹ (**Figure S26**). The unstructured N-terminal signal sequence (residue 1-34) was excluded. To predict which regions of the protein may play a role in lipid packing defect sensing, a previously developed neural network model was applied.⁵⁴ A sliding window of 15 residues was used to predict binding free energy values ($\Delta\Delta F$) for peptide motifs along the sequence of the bovine LPL protein (sections **S17-S19**). In order to exclude buried protein regions (that are unavailable to interact with membranes), only peptide motifs with an average solvent-accessible surface area (SASA, as calculated using BioPython⁷⁴) of greater than 0.8 nm² were considered. To visualize putative regions of interest, the B-factor field in the PDB file format was used to adjust the coloring accordingly.

Umbrella sampling: A DSPC bilayer (361 molecules per leaflet) was prepared using the *insane* python script⁷⁵ and the Martini 3 CG force field.⁴⁸ After solvation with Martini 3 water and ions (0.15 M NaCl), steepest decent energy minimization and 10 ns of semiisotropic NpT equilibration ($p_{\text{ref}} = 1$ bar) were performed. Next, a layer of 1444 randomly oriented DOaG molecules was inserted between the two DSPC leaflets. The resulting 1:2 DSPC:DOaG membrane was energy minimized and equilibrated. A 75 bar·nm surface tension was applied to the membrane system to match the lipid packing defects (measured with a protocol based on PackMem (same as the one calculating defects on the spherical droplet and with the recommended settings⁷¹) to the ones found on a DSPC/DOaG spherical lipid droplet (see **Figure S16**). A CG Martini representation of the LPL protein was obtained with Martinize2/VerMOUTH.⁷⁶ Secondary structure was predicted with DSSP⁷⁷ and constrained by an elastic network between the backbone beads ($k_{\text{force}} =$

500 kJ mol⁻¹). The CG protein was inserted into the DSPC or DSPC/DOaG systems with ~4 nm separation between the Trp-rich loop of the protein (Ile413-Pro427) and the upper leaflet's lipid head groups. The resulting set-ups were resolvated with water and ions (0.15 M NaCl). After steepest decent energy minimization, both systems were equilibrated for 100 ns with position restraints ($k_{\text{force}} = 1,000 \text{ kJ mol}^{-1}$) on all protein beads. The initial frames for US were generated by running a pulling simulation in which the z-distance between the centers-of-mass (COM) of the Trp-rich loop and the lipids was decreased gradually, and then selecting 24 frames that span the range from the solvated to the membrane-bound state with 0.2 nm increments. For each umbrella window, a 50 ns equilibration followed by a 2 μs production run was performed in which the Lipid-Trp-rich loop COM z-distance was constrained to its initial value ($k_{\text{force}} = 500 \text{ kJ mol}^{-1}$). To dampen membrane deformations during US runs, a soft harmonic flat-bottom potential ($k_{\text{force}} = 100 \text{ kJ mol}^{-1}$) was applied on the lipid head groups to restrain the lipids within its initial thickness range (+0.5 nm on each side of the membrane). Free energy profiles were obtained through umbrella integration⁷⁸ with 10,000 bins. Averages and standard deviations were calculated by using block-averaging over 3 blocks.

Mass spectrometry analysis: DSPC and DOaG were analyzed by Liquid Chromatography tandem Mass Spectrometry (LC-MS/MS). Solutions of DSPC and DOaG (1 pmol/ μL) were prepared in 5 mM ammonium formate, in methanol. The compounds were introduced in the mass spectrometer and the tuning conditions for both compounds were determined as indicated below.

Lipid extraction: For the MS analysis and for each time point, 9 μL of each sample (PAP3 liposomes incubating at 37 °C with or without LPL) was flush frozen in liquid nitrogen to ensure discontinuation of the hydrolysis. Subsequently the samples were extracted by a modified Bligh and Dyer extraction⁷⁹ using acidic buffer (100 mM ammonium formate buffer, pH = 3.1). Briefly, in an Eppendorf tube, 400 μL methanol and 200 μL of chloroform were added to the sample. The sample was vortexed for 30 min at room temperature and centrifuged for 10 min at 15,700 g to spin down precipitated protein.

MS/MS parameters

Mass Spectrometer	Xevo TQ-S micro (Waters)				
Capillary voltage	3.50 kV				
Source temperature	150°C				
Desolvation temperature	450°C				
Cone gas	50 L/h				
Desolvation gas	950 L/h				
Compound	Retention time (min)	Parent (m/z)	Daughter (m/z)	Cone Voltage (V)	Collision energy (V)
DOaG	2.51	620.9	602.9	15	15
DSPC	4.45	790.7	184.0	15	20

The supernatant was transferred to a new Eppendorf tube and 200 μ L chloroform and 350 μ L water were added for extraction of the lipids. After centrifugation (5 min at 15,700 g), the lower (organic) phase was transferred to a clean Eppendorf tube and the upper (aqueous) phase was re-extracted by adding 400 μ L of chloroform. Organic phases were pooled and taken to dryness at 45 °C under a nitrogen stream. Next, the residue was dissolved in 600 μ L of butanol and 600 μ L of water, mixed and centrifuged for 10 min at 15,700 g. The butanol phase was transferred to a clean tube and taken to dryness in Eppendorf Concentrator Plus at 45 °C. The residue was dissolved in 100 μ L methanol, stirred and sonicated in a bath for 30 s and centrifuged for 10 min at 15,700 \times g. Finally, 10 μ L of the supernatant was applied to the UPLC-MS/MS. Data are the average of 2 experiments.

LC-MS/MS: Measurements were performed by reverse-phase liquid chromatography using a Waters UPLC-Xevo-TQS micro and a BEH C18 column, 2.1 \times 50 mm with 1.7 μ m particle size (Waters, USA), by applying an isocratic elution of methanol containing 10 mM ammonium formate. The UPLC program was applied for 7 min at a flow rate of 0.250 mL/min. The temperature of the column and of the autosampler were kept at 23 °C and 10 °C, respectively, during the run. Data were analyzed with Masslynx 4.2 Software (Waters Corporation; Milford MA).

3.5 Supplementary Information

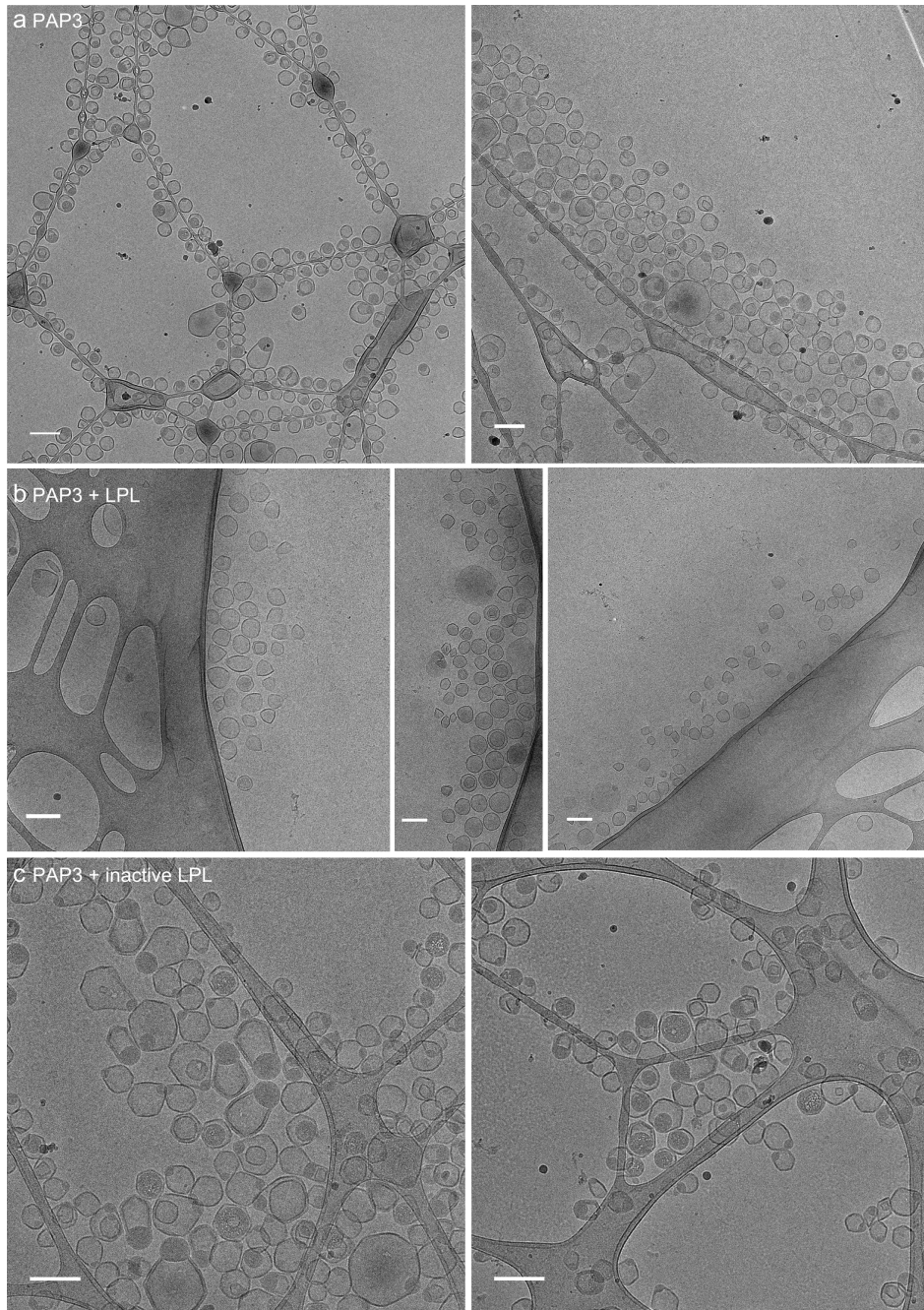


Figure S1. Cryo-TEM images of PAP3 liposomes a) without LPL, b) with LPL and c) with inactive LPL incubating for 180 min at 37 °C. Images as chosen for quantification of the whole population. Scale bars: 200 nm.

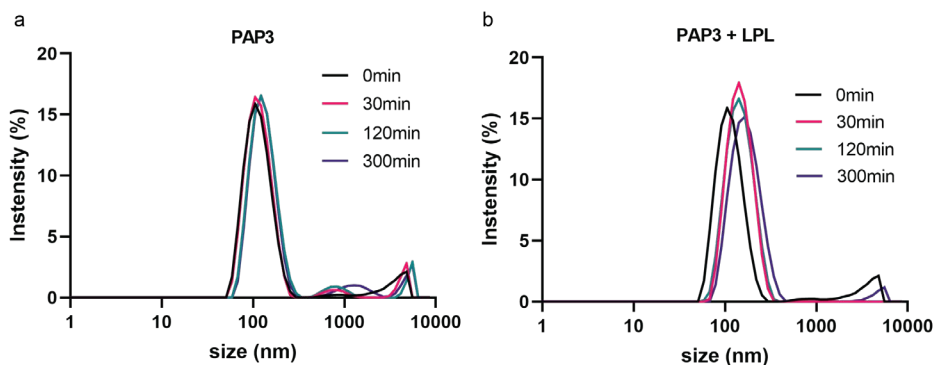


Figure S2. Size of PAP3 liposomes overtime as measured by dynamic light scattering (DLS). a) before and b) after addition of LPL. Liposomes incubating at 37 °C for 0, 30, 120 and 300 min.

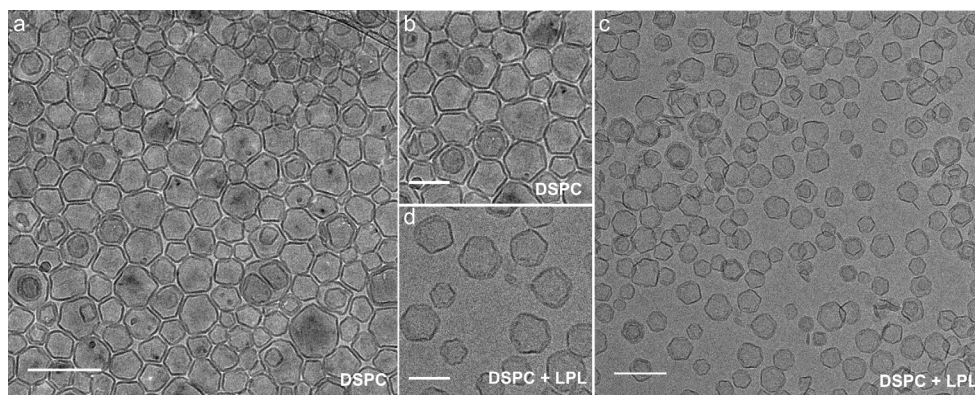


Figure S3. Cryo-TEM images of DSPC liposomes a, b) before and c, d) after addition of LPL. Liposomes incubating at 37 °C for 180 min. Scale bars: 200 nm for a, c and 100 nm for b, d.

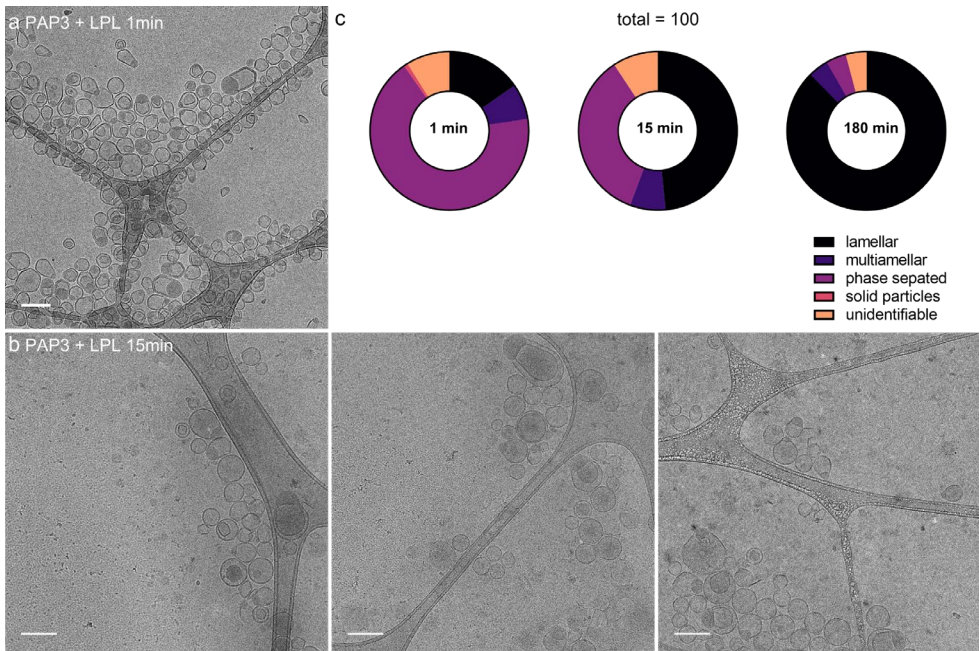


Figure S4. Cryo-TEM images of PAP3 liposomes with LPL incubating at 37°C for a) 1 min or b) 15 min and c) Quantification of the whole population of PAP3 liposomes with LPL incubating at 37 °C for 1, 15 and 180 min. Images as chosen for quantification. Scale bars: 200 nm.

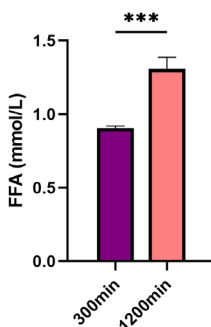


Figure S5. Release of FFA from PAP3 liposomes incubating with LPL. PAP3 liposomes incubating at 37 °C with LPL for 300 and 1200 min. Statistical significance was evaluated using a two-tailed unpaired Student's t-test. ns: not significant ($P > 0.05$). Significantly different: * $P \leq 0.05$, ** $P \leq 0.01$; *** $P < 0.001$. Exact P value 0.0009.

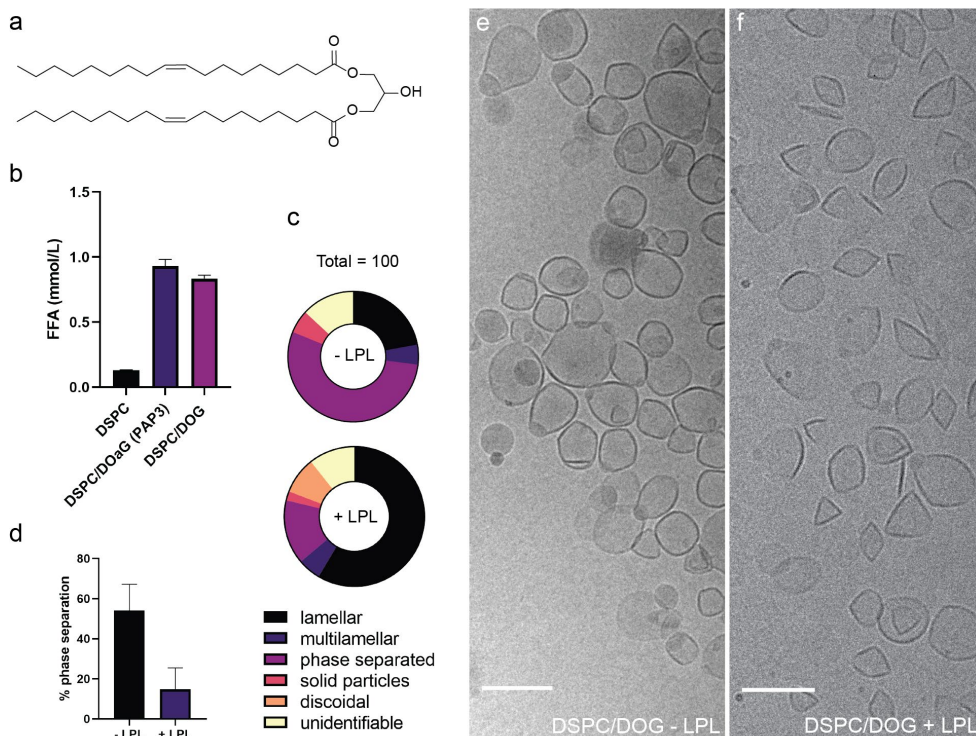


Figure S6. Effect of LPL on DOG containing liposomes. **a**) Molecular structure of dioleoylglycerol (DOG). **b**) Release of FFA from liposomes containing DSPC (100%), DSPC/DOaG (1:1), or DSPC/DOG (1:1) after incubation with LPL at 37 °C for 120 min. **c**) Quantification (N=100) of the whole population of liposomes consisting of DSPC/DOG (1:1) without LPL or with LPL, incubating at 37 °C for 120 min. **d**) Percentage of phase separation of liposomes consisting of DSPC/DOG (1:1) incubating at 37 °C for 120 min without or with LPL. **e**) Cryo-TEM images of liposomes consisting of DSPC/DOG (1:1) incubating at 37 °C for 120 min without LPL and **f**) with LPL. Scale bars: 200 nm.

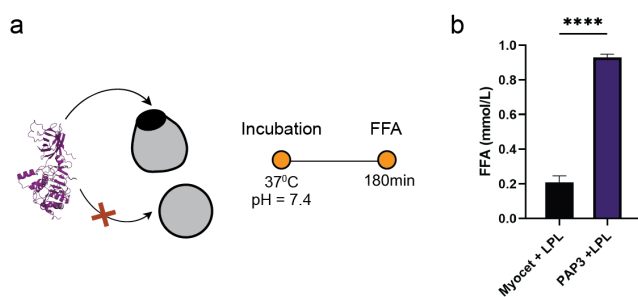


Figure S7. Release of FFA from Myocet[®]-based formulation in comparison to PAP3 liposomes. **a**) Schematic of LPL interacting with PAP3 or Myocet[®]-like liposomes and

timeline of measurement of released FFA. **b)** Quantification of released FFA from Myocet[®]-like or PAP3 liposomes after incubating with LPL at 37 °C for 180 min. Statistical significance was evaluated using a two-tailed unpaired Student's t-test. ns: not significant ($P > 0.05$). Significantly different: * $P \leq 0.05$, ** $P \leq 0.01$; *** $P < 0.001$, **** $P < 0.0001$. Exact P value : < 0.0001.

			DOaG/DSPC	% Abundance
PAP3	.-LPL	t = 0h	0,830483	86,50863
PAP3	.-LPL	t = 0h	0,977713	101,8451
PAP3	+.LPL	t = 0h	1,046577	109,0185
PAP3	+.LPL	t = 0h	0,984694	102,5723
PAP3	.-LPL	t = 3h	0,932472	97,13248
PAP3	.-LPL	t = 3h	0,950282	98,98767
PAP3	+.LPL	t = 3h	0,753585	78,49848
PAP3	+.LPL	t = 3h	0,65356	68,07916

Figure S8. Mass spectrometry analysis of PAP3 liposomes (DOaG:DSPC 1:1). Analysis table of DOaG/DSPC ratio before and after addition of LPL at $t = 0$ h and $t = 3$ h (at 37 °C). Abundance (%) was determined by normalizing all PAP3 data against PAP3 at $t = 0$ h (average of the two measurements was set as 100%).

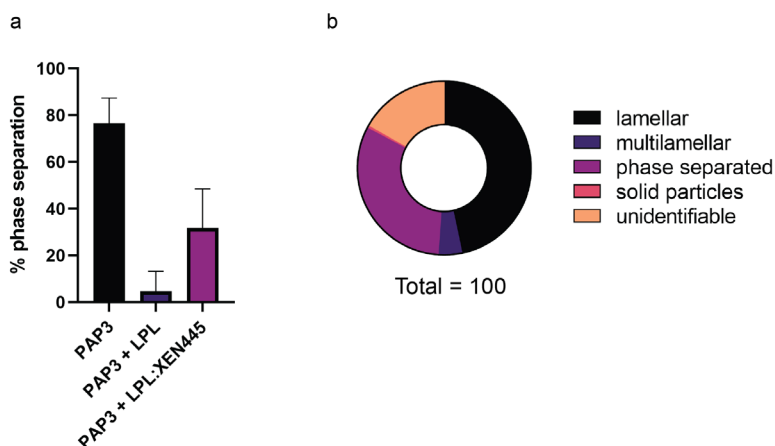
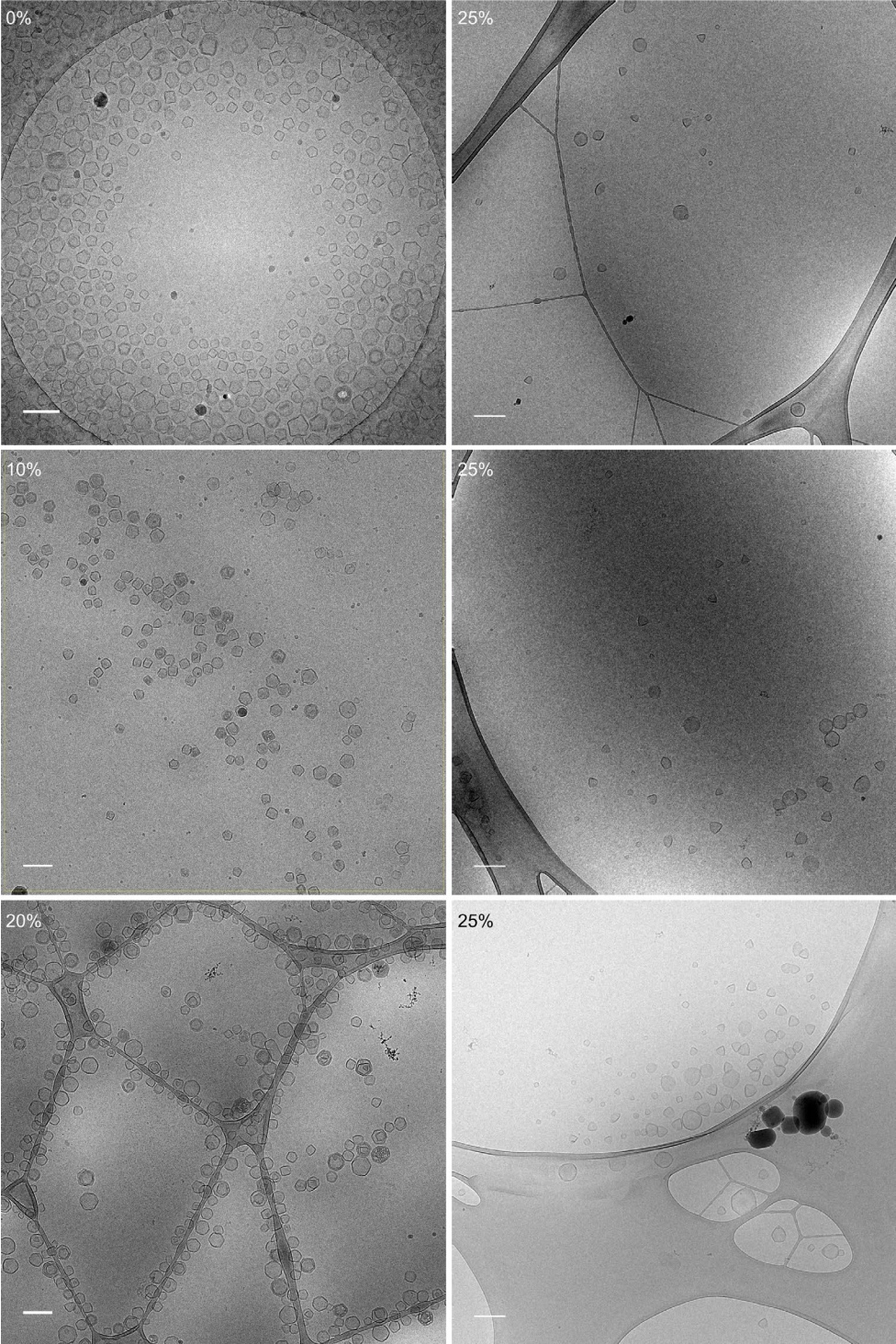


Figure S9. Effect of XEN445 on LPL lipolytic activity. **a)** Percentage of phase separation of PAP3 liposomes incubating at 37 °C for 120 min without, or with LPL, or with LPL after addition of 1000 μ M XEN445 inhibitor. **b)** Quantification of all populations found on PAP3 liposomal formulation incubating with LPL for 120 min after addition of 1000 μ M XEN445 inhibitor. Quantification based on cryo-TEM particle count ($N=200$).



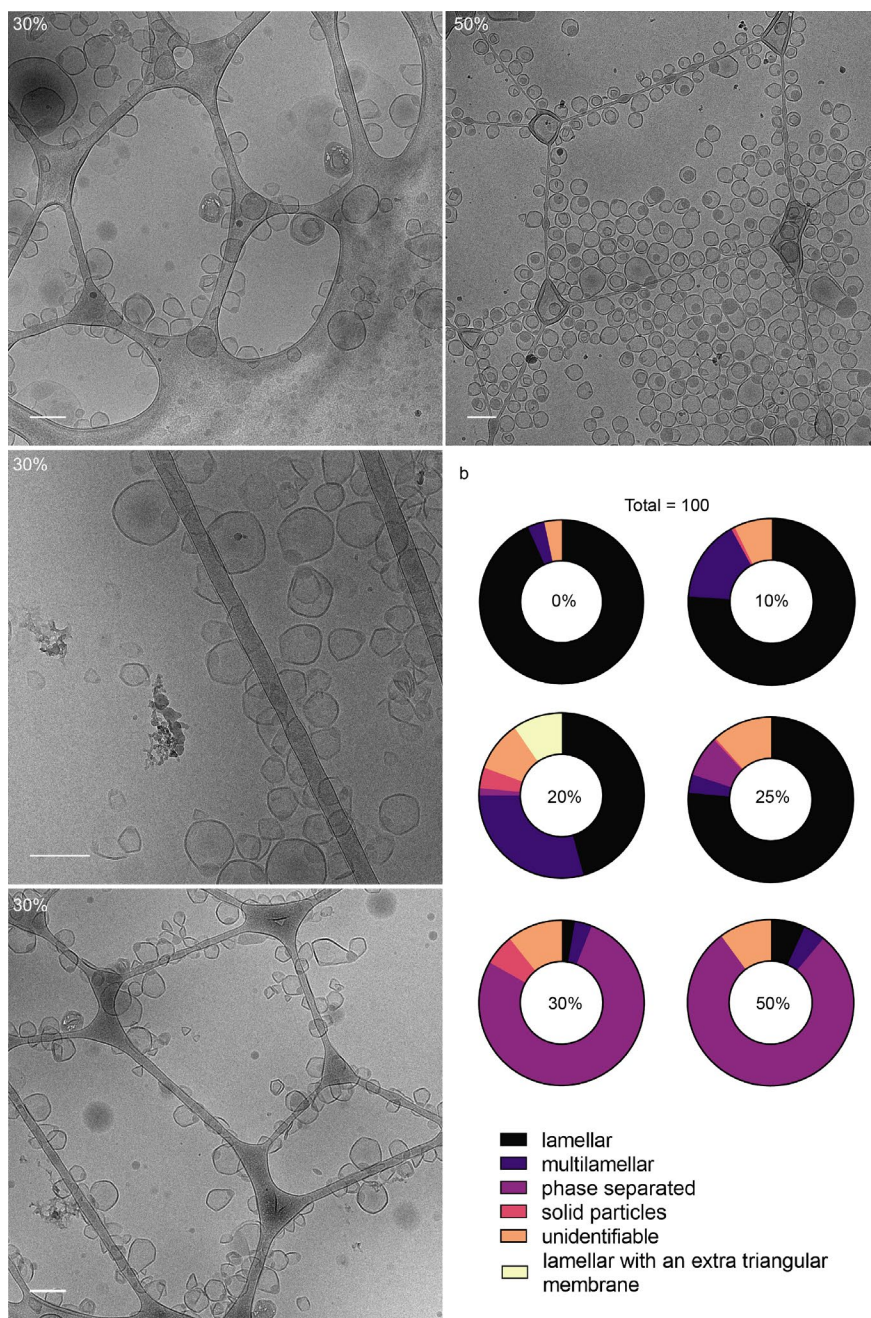


Figure S10. Cryo-TEM images and quantification of PAP3 liposomes formulated at varying molar ratios. a) Cryo-TEM images of liposomes composed of DSPC and 0, 20, 25, 30 and 50 mol % DOaG. Images as chosen for quantification of the whole population. Scale bars: 200 nm. b) Quantification of the whole population. Total of each circle chart = 100. Quantification based on cryo-TEM particle count (N=200).

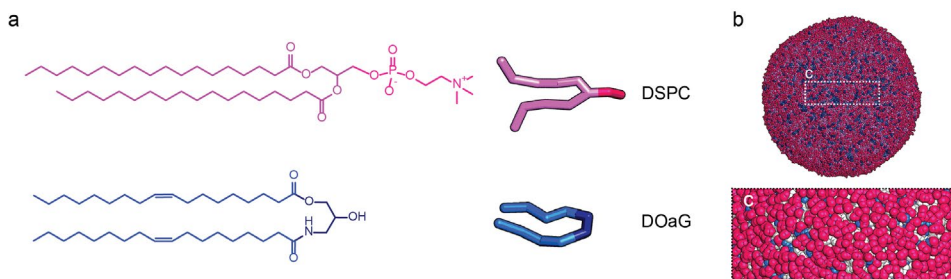


Figure S11. Lipids used for the coarse-grained representation of PAP3 liposomes. a) Molecular structures of DSPC and DOaG lipids and simulated representations. b) Modeled lipid droplet of PAP3 liposomes. c) Zoom in of b showing the lipid packing defects and the high spacing between DSPC headgroups exposing the DOaG (grey/blue). Size of droplet radius 20.1 nm.

SI 12 Coarse-Grained model

While several lipids have been parametrised within the Martini context, including DSPC, a representation of DOaG is lacking and should be parametrised. Our starting point is an existing representation for a diacylglycerol lipid (DOG), which is very similar to DOaG. Observations by cryo-TEM are used as a reference, and indicate that phase-separated liposomes are formed for mixtures containing > 25 %mol of DOaG, assuming that DOaG is evenly distributed over all liposomes. The ambiguity in the CG representation of DOaG is in the choice of the head beads, *i.e.*, in the non-bonded interactions that are usually estimated from relative partitioning in two different solvents, and we may use the experimental data for phase separation as an alternative. To quantify phase separation *in silico*, the contact fraction between DOaG and DSPC is used:

$$f_{DOaG-DSPC} = \frac{c_{DOaG-DMPC}}{c_{DOaG-DMPC} + c_{DOaG-DOaG}} \times \frac{1}{\phi_{DOaG}}$$

with c_{i-j} representing the number of contacts between two lipid species, and ϕ_{DOaG} the fraction of DOaG lipids. The normalisation by the DOaG fraction, which is not used in the original formulation,⁸⁰ is introduced to enable a direct comparison of membranes with different fractions of DOaG, *i.e.*, by normalizing the maximum of the contact fraction to unity. To determine if two lipids are in direct contact, the standard distance threshold of 1.1 nm was used for the GL1 bead (if the lipid is a DSPC lipid) and the GLA bead (in case of DOaG). Density profiles (see **Figure S13**) along the membrane normal indicate that these beads reside roughly at the same depth within the monolayer.

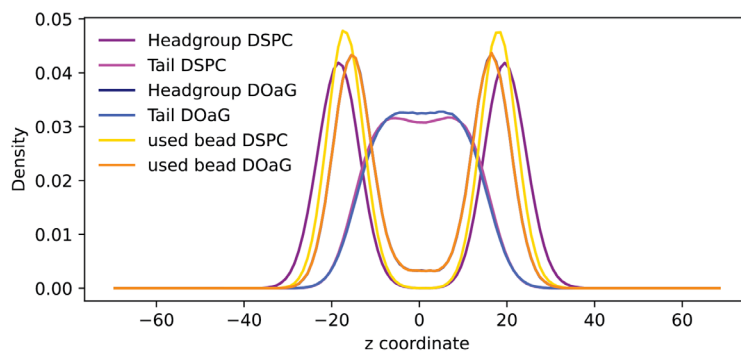


Figure S13. Density profiles of selected bead types across the membrane (along the normal). The contact fraction was subsequently employed to monitor the degree of phase separation for varying DOaG fractions and for different bead-type representations of the DOaG head group in CG Martini. We considered both Martini 2 and 3. Based on the best fit to the experimental data, the DOaG representation with N6a and N6d beads was selected as most appropriate. DPPC = DSPC.

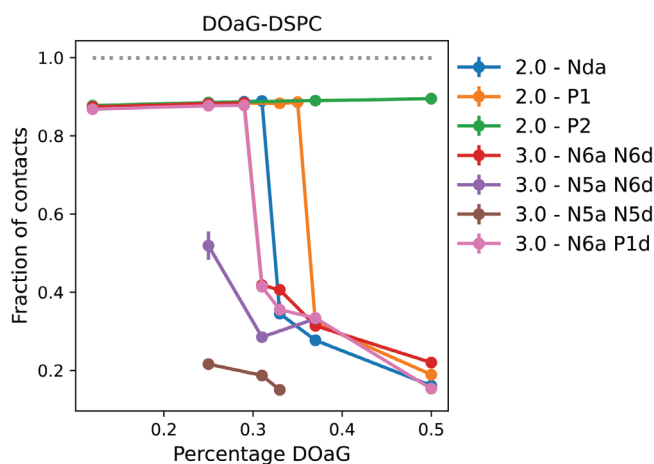


Figure S14. Fractions of contact for increasing composition fractions of DOaG as calculated from CG membrane simulations. Contact fractions have been determined by averaging over the last μs of a $2 \mu\text{s}$ simulation trajectory.

SI 15. Input file for the CG Martini representation for DOaG used in this study:

```

[moleculetype]; molname  nrexcl
DOAG      1

[atoms]; id      type    resnr  residu  atom  cgnr
  1     N6a     1     DOAG  GLA   1     0
  2     N6d     1     DOAG  NAB   2     0
  3     C1      1     DOAG  C1A   3     0
  4     C4h     1     DOAG  D2A   4     0
  5     C1      1     DOAG  C3A   5     0
  6     C1      1     DOAG  C4A   6     0
  7     C1      1     DOAG  C1B   7     0
  8     C4h     1     DOAG  D2B   8     0
  9     C1      1     DOAG  C3B   9     0
 10     C1      1     DOAG  C4B  10     0

[bonds];
i      j      funct  length  force.c.
  1  2      1      0.312  2500
  1  3      1      0.47   5000
  3  4      1      0.47   3800
  4  5      1      0.47   3800
  5  6      1      0.47   3800
  2  7      1      0.47   3600
  7  8      1      0.47   3800
  8  9      1      0.47   3800
  9 10      1      0.47   3800

[angles];
i  j  k  funct  angle  force.c.
  1  3  4  2     180.0  35.0
  3  4  5  2     120.0  35.0
  4  5  6  2     180.0  35.0
  2  7  8  2     180.0  35.0
  7  8  9  2     120.0  35.0
  8  9 10  2     180.0  35.0

```

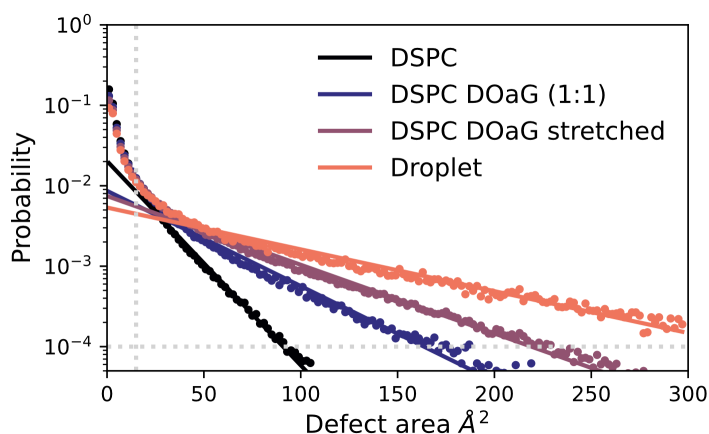


Figure S16. Standard practice when using PackMem is retrieving the packing defect constant from fitting the probability to find a defect of a certain area. This probability of finding a defect of a certain area is given by the formula: $P(A) = b e^{-\frac{A}{\pi}}$, where $P(A)$ is the probability of finding a defect area of area \AA^2 , b is a constant and π is the packing defect constant. The fit is performed on all datapoints where the area of the defect is bigger than 15\AA^2 and the probability is higher than $1e^{-4}$. The fit for the flat DSPC, flat but phase-separated DSPC/DOaG layer (1:1 ratio), for the stretched phase-separated DSPC/DOaG layer and spherical DSPC/DOaG system (droplet), are shown in this figure. The solid line of the same color is the fit through the data, which gives the packing defect constant for each system.

SI 17 Identifying lipid packing defect sensing motifs on LPL protein structure

Our previously developed neural network (NN) model is able to predict the relative free energy of a peptide binding to a stretched membrane (high packing defect constant) versus a tensionless membrane (low packing defect constant),⁵⁴ only requiring the amino acid sequence. To identify putative regions with lipid packing defect sensing ability within a 3D protein structure of LPL, we used a python script that employs a sliding window of length 15 to screen the protein sequence and predict $\Delta\Delta F$ for every segment. Since the segments overlap, every individual residue is part of more than one segment (except for the termini). By taking the average of these overlapping segment scores at every position we obtained a “per-residue” $\Delta\Delta F$ which can be interpreted as the contribution of that single amino acid to the overall lipid packing defect sensing ability of the respective protein region (**Figure S18a**).

For a residue to bind to a membrane's lipid packing defects, it must be located at the outer shell of the protein structure, *i.e.*, it must be exposed to the solvent. We accounted for this by calculating the solvent-accessible surface area (SASA) for every individual residue (using BioPython)⁷⁴, based on the 3D protein structure. Then, we calculated the average SASA of the direct vicinity: a 9 amino acid stretch ($n_{-4} - n_{+4}$) around the respective residue at position n (**Figure S18b**). If this averaged SASA exceeded a threshold value of 0.8 nm^2 , we considered that residue to be sufficiently solvent exposed to potentially contribute to lipid packing defect sensing ability. If not, that residue was labeled inactive.

By taking both the averaged per-residue $\Delta\Delta F$ and SASA values into account, we mapped and color-coded the predicted lipid packing defect sensing ability onto the 3D protein structure, as we show in **Figure 5b** in the main text. For this, we used the B-factor field in the PDB file, applying the following rules:

$$\begin{aligned} \text{if SASA} < 0.8: & \quad Bfactor = 0.0 \\ \text{if SASA} \geq 0.8: & \quad Bfactor = \frac{x - x_{max}}{x_{min} - x_{max}} \times 100 \end{aligned}$$

In which x is the per-residue $\Delta\Delta F$ score and x_{max} and x_{min} are the maximal and minimal value of x for the entire protein. This formula yields a maximal B-factor of 100.0 for the highest score (most negative $\Delta\Delta F$, $x=x_{min}$) and the minimal B-factor of 0.0 for the lowest score ($x=x_{max}$). Note that $\Delta\Delta F$ values are always negative.

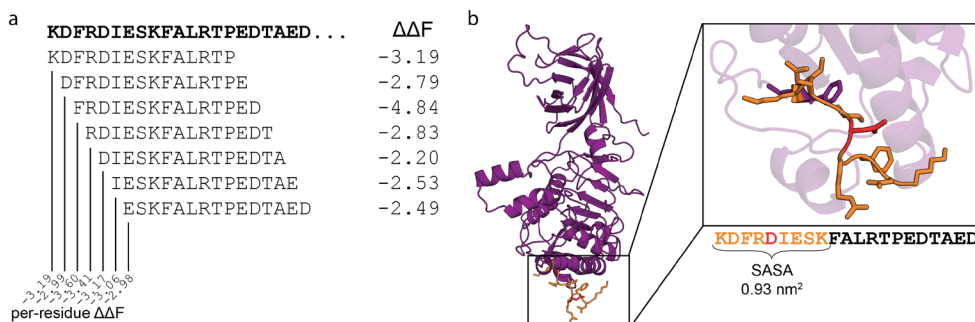


Figure S18. a) An example of NN-predicted $\Delta\Delta F$ values for overlapping 15-residue fragments of LPL (*Bos Taurus*) N-terminal region. The average of the overlapping scores yields the per-residue $\Delta\Delta F$ at every position. b) For every amino acid in the 3D protein structure, the individual SASA is calculated. Then, for every position, we compute the average SASA of the 9-residue vicinity (in orange) and assign that value (0.93 nm^2 in this case) to the middle residue (Asp39 in this example, in red).

S19 Residue scores. Per-residue SASA, $\Delta\Delta F$, and resulting B-factors for LPL (*Bos Taurus*).

		SASA	$\Delta\Delta F$	B-factor
35	K	1.20	-3.19	22.20
36	D	1.05	-2.99	17.42
37	F	1.04	-3.60	31.98
38	R	0.92	-3.41	27.45
39	D	0.93	-3.17	21.72
40	I	0.73	-3.06	0.00
41	E	0.64	-2.98	0.00
42	S	0.61	-3.00	0.00
43	K	0.39	-3.00	0.00
44	F	0.34	-3.06	0.00
45	A	0.39	-3.00	0.00
46	L	0.46	-3.05	0.00
47	R	0.50	-3.05	0.00
48	T	0.42	-3.06	0.00
49	P	0.47	-3.08	0.00
50	E	0.59	-3.08	0.00
51	D	0.62	-3.09	0.00
52	T	0.73	-2.94	0.00
53	A	0.71	-2.97	0.00
54	E	0.70	-3.05	0.00
55	D	0.52	-3.10	0.00
56	T	0.56	-3.16	0.00
57	C	0.55	-3.20	0.00
58	H	0.55	-3.29	0.00
59	L	0.49	-3.41	0.00
60	I	0.50	-3.46	0.00
61	P	0.51	-3.51	0.00
62	G	0.48	-3.45	0.00
63	V	0.42	-3.45	0.00
64	T	0.49	-3.37	0.00
65	E	0.52	-3.44	0.00
66	S	0.51	-3.44	0.00
67	V	0.63	-3.51	0.00
68	A	0.59	-3.61	0.00
69	N	0.60	-3.78	0.00
70	C	0.57	-3.91	0.00
71	H	0.68	-4.06	0.00
72	F	0.70	-4.17	0.00
73	N	0.69	-4.15	0.00
74	H	0.57	-4.05	0.00
75	S	0.56	-4.16	0.00

		SASA	$\Delta\Delta F$	B-factor
90	M	0.54	-4.92	0.00
91	Y	0.54	-5.02	0.00
92	E	0.48	-5.01	0.00
93	S	0.49	-5.08	0.00
94	W	0.47	-5.05	0.00
95	V	0.33	-5.06	0.00
96	P	0.31	-5.05	0.00
97	K	0.27	-5.05	0.00
98	L	0.20	-5.09	0.00
99	V	0.22	-5.01	0.00
100	A	0.39	-4.94	0.00
101	A	0.41	-4.82	0.00
102	L	0.34	-4.76	0.00
103	Y	0.43	-4.62	0.00
104	K	0.55	-4.35	0.00
105	R	0.52	-4.13	0.00
106	E	0.52	-3.90	0.00
107	P	0.52	-3.82	0.00
108	D	0.50	-3.65	0.00
109	S	0.33	-3.64	0.00
110	N	0.28	-3.61	0.00
111	V	0.27	-3.77	0.00
112	I	0.19	-3.90	0.00
113	V	0.09	-4.01	0.00
114	V	0.15	-4.18	0.00
115	D	0.16	-4.28	0.00
116	W	0.16	-4.47	0.00
117	L	0.26	-4.47	0.00
118	S	0.35	-4.41	0.00
119	R	0.50	-4.40	0.00
120	A	0.52	-4.37	0.00
121	Q	0.59	-4.38	0.00
122	Q	0.64	-4.29	0.00
123	H	0.57	-4.26	0.00
124	Y	0.56	-4.17	0.00
125	P	0.60	-4.04	0.00
126	V	0.59	-3.76	0.00
127	S	0.50	-3.56	0.00
128	A	0.46	-3.48	0.00
129	G	0.48	-3.32	0.00
130	Y	0.41	-3.31	0.00

76	S	0.39	-4.21	0.00
77	K	0.37	-4.42	0.00
78	T	0.31	-4.55	0.00
79	F	0.23	-4.73	0.00
80	V	0.11	-4.77	0.00
81	V	0.18	-4.86	0.00
82	I	0.11	-4.88	0.00
83	H	0.20	-4.76	0.00
84	G	0.30	-4.64	0.00
85	W	0.32	-4.57	0.00
86	T	0.45	-4.49	0.00
87	V	0.53	-4.44	0.00
88	T	0.56	-4.54	0.00
89	G	0.62	-4.77	0.00
		SASA	$\Delta\Delta F$	B-factor
145	M	0.33	-5.62	0.00
146	A	0.48	-5.54	0.00
147	D	0.48	-5.46	0.00
148	E	0.53	-5.45	0.00
149	F	0.52	-5.70	0.00
150	N	0.57	-5.73	0.00
151	Y	0.60	-5.77	0.00
152	P	0.51	-5.71	0.00
153	L	0.42	-5.62	0.00
154	G	0.36	-5.46	0.00
155	N	0.22	-5.28	0.00
156	V	0.21	-5.27	0.00
157	H	0.15	-5.26	0.00
158	L	0.15	-5.31	0.00
159	L	0.10	-5.37	0.00
160	G	0.04	-5.37	0.00
161	Y	0.04	-5.55	0.00
162	S	0.02	-5.55	0.00
163	L	0.02	-5.58	0.00
164	G	0.02	-5.29	0.00
165	A	0.02	-5.15	0.00
166	H	0.02	-4.90	0.00
167	A	0.01	-4.78	0.00
168	A	0.02	-4.59	0.00
169	G	0.09	-4.47	0.00
170	I	0.17	-4.38	0.00
171	A	0.20	-4.08	0.00
172	G	0.31	-3.93	0.00

131	T	0.33	-3.25	0.00
132	K	0.42	-3.43	0.00
133	L	0.42	-3.55	0.00
134	V	0.38	-3.65	0.00
135	G	0.30	-3.76	0.00
136	Q	0.37	-3.92	0.00
137	D	0.26	-4.10	0.00
138	V	0.19	-4.34	0.00
139	A	0.21	-4.57	0.00
140	K	0.23	-4.87	0.00
141	F	0.13	-5.19	0.00
142	M	0.15	-5.34	0.00
143	N	0.24	-5.42	0.00
144	W	0.35	-5.56	0.00
		SASA	$\Delta\Delta F$	B-factor
200	R	0.56	-3.33	0.00
201	L	0.41	-3.22	0.00
202	S	0.37	-3.04	0.00
203	P	0.33	-2.94	0.00
204	D	0.29	-2.85	0.00
205	D	0.26	-2.75	0.00
206	A	0.27	-2.95	0.00
207	D	0.27	-2.95	0.00
208	F	0.22	-3.11	0.00
209	V	0.10	-3.10	0.00
210	D	0.09	-3.19	0.00
211	V	0.11	-3.26	0.00
212	L	0.06	-3.36	0.00
213	H	0.25	-3.38	0.00
214	T	0.30	-3.41	0.00
215	F	0.35	-3.45	0.00
216	T	0.43	-3.40	0.00
217	R	0.44	-3.38	0.00
218	G	0.67	-3.34	0.00
219	S	0.67	-3.34	0.00
220	P	0.72	-3.32	0.00
221	G	0.71	-3.13	0.00
222	R	0.51	-2.96	0.00
223	S	0.51	-2.91	0.00
224	I	0.52	-2.99	0.00
225	G	0.49	-2.98	0.00
226	I	0.47	-3.05	0.00
227	Q	0.25	-3.03	0.00

173	S	0.47	-3.70	0.00
174	L	0.57	-3.53	0.00
175	T	0.56	-3.33	0.00
176	N	0.61	-3.10	0.00
177	K	0.61	-2.92	0.00
178	K	0.54	-2.82	0.00
179	V	0.45	-2.72	0.00
180	N	0.43	-2.76	0.00
181	R	0.32	-2.84	0.00
182	I	0.16	-2.90	0.00
183	T	0.06	-2.93	0.00
184	G	0.06	-3.10	0.00
185	L	0.01	-3.19	0.00
186	D	0.04	-3.36	0.00
187	P	0.15	-3.50	0.00
188	A	0.15	-3.63	0.00
189	G	0.17	-3.70	0.00
190	P	0.34	-3.80	0.00
191	N	0.36	-3.81	0.00
192	F	0.52	-3.95	0.00
193	E	0.55	-3.89	0.00
194	Y	0.66	-3.94	0.00
195	A	0.66	-3.83	0.00
196	E	0.59	-3.73	0.00
197	A	0.58	-3.67	0.00
198	P	0.57	-3.63	0.00
199	S	0.45	-3.46	0.00
		SASA	$\Delta\Delta F$	B-factor
255	I	0.84	-3.66	33.41
256	A	0.98	-3.49	29.36
257	E	0.96	-3.27	24.11
258	R	0.93	-3.10	20.05
259	G	0.95	-2.97	16.95
260	L	0.98	-2.94	16.23
261	G	1.00	-2.83	13.60
262	D	0.92	-2.70	10.50
263	V	0.79	-2.65	0.00
264	D	0.79	-2.59	0.00
265	Q	0.68	-2.69	0.00
266	L	0.58	-2.69	0.00
267	V	0.51	-2.67	0.00
268	K	0.46	-2.67	0.00
269	C	0.38	-2.72	0.00

228	K	0.26	-3.17	0.00
229	P	0.19	-3.24	0.00
230	V	0.19	-3.28	0.00
231	G	0.19	-3.35	0.00
232	H	0.15	-3.42	0.00
233	V	0.08	-3.45	0.00
234	D	0.06	-3.57	0.00
235	I	0.07	-3.70	0.00
236	Y	0.07	-3.77	0.00
237	P	0.10	-3.82	0.00
238	N	0.16	-3.85	0.00
239	G	0.16	-3.79	0.00
240	G	0.21	-3.77	0.00
241	T	0.25	-3.79	0.00
242	F	0.26	-3.92	0.00
243	Q	0.32	-3.94	0.00
244	P	0.46	-3.96	0.00
245	G	0.51	-3.99	0.00
246	C	0.53	-4.01	0.00
247	N	0.48	-4.05	0.00
248	I	0.60	-4.06	0.00
249	G	0.67	-3.99	0.00
250	E	0.68	-3.86	0.00
251	A	0.73	-3.82	0.00
252	L	0.73	-3.82	0.00
253	R	0.72	-3.73	0.00
254	V	0.87	-3.72	34.84
		SASA	$\Delta\Delta F$	B-factor
310	K	0.70	-2.69	0.00
311	N	0.71	-2.66	0.00
312	R	0.69	-2.61	0.00
313	C	0.65	-2.54	0.00
314	N	0.52	-2.48	0.00
315	N	0.37	-2.42	0.00
316	M	0.29	-2.40	0.00
317	G	0.25	-2.31	0.00
318	Y	0.35	-2.29	0.00
319	E	0.39	-2.26	0.00
320	I	0.53	-2.27	0.00
321	N	0.59	-2.26	0.00
322	K	0.82	-2.26	0.00
323	V	1.01	-2.29	0.72
324	R	1.01	-2.32	1.43

270	S	0.27	-2.81	0.00
271	H	0.22	-2.93	0.00
272	E	0.17	-3.00	0.00
273	R	0.13	-3.09	0.00
274	S	0.09	-3.23	0.00
275	V	0.10	-3.34	0.00
276	H	0.10	-3.48	0.00
277	L	0.08	-3.68	0.00
278	F	0.08	-3.78	0.00
279	I	0.15	-3.79	0.00
280	D	0.21	-3.72	0.00
281	S	0.28	-3.67	0.00
282	L	0.47	-3.70	0.00
283	L	0.57	-3.69	0.00
284	N	0.59	-3.56	0.00
285	E	0.59	-3.48	0.00
286	E	0.65	-3.47	0.00
287	N	0.64	-3.47	0.00
288	P	0.56	-3.44	0.00
289	S	0.62	-3.31	0.00
290	K	0.53	-3.17	0.00
291	A	0.51	-3.11	0.00
292	Y	0.44	-2.99	0.00
293	R	0.50	-2.95	0.00
294	C	0.59	-2.88	0.00
295	N	0.55	-2.86	0.00
296	S	0.55	-2.89	0.00
297	K	0.64	-2.84	0.00
298	E	0.65	-2.87	0.00
299	A	0.63	-2.94	0.00
300	F	0.58	-2.96	0.00
301	E	0.57	-2.88	0.00
302	K	0.49	-2.91	0.00
303	G	0.42	-2.88	0.00
304	L	0.43	-2.96	0.00
305	C	0.59	-2.92	0.00
306	L	0.71	-2.86	0.00
307	S	0.68	-2.80	0.00
308	C	0.81	-2.70	10.50
309	R	0.72	-2.68	0.00

325	A	1.01	-2.35	2.15
326	K	1.00	-2.40	3.34
327	R	0.89	-2.58	7.64
328	S	0.85	-2.64	9.07
329	S	0.69	-2.79	0.00
330	K	0.66	-2.98	0.00
331	M	0.43	-3.26	0.00
332	Y	0.29	-3.37	0.00
333	L	0.29	-3.52	0.00
334	K	0.42	-3.55	0.00
335	T	0.43	-3.73	0.00
336	R	0.51	-3.86	0.00
337	S	0.51	-4.09	0.00
338	Q	0.57	-4.33	0.00
339	M	0.55	-4.62	0.00
340	P	0.57	-4.82	0.00
341	Y	0.50	-4.94	0.00
342	K	0.45	-4.90	0.00
343	V	0.33	-4.98	0.00
344	F	0.24	-5.04	0.00
345	H	0.25	-4.88	0.00
346	Y	0.23	-4.68	0.00
347	Q	0.26	-4.58	0.00
348	V	0.25	-4.47	0.00
349	K	0.25	-4.43	0.00
350	I	0.27	-4.26	0.00
351	H	0.42	-4.20	0.00
352	F	0.53	-4.01	0.00
353	S	0.66	-3.80	0.00
354	G	0.63	-3.50	0.00
355	T	0.72	-3.30	0.00
356	E	0.71	-3.11	0.00
357	S	0.81	-3.07	19.33
358	N	0.91	-2.97	16.95
359	T	0.90	-2.89	15.04
360	Y	0.77	-2.95	0.00
361	T	0.64	-2.93	0.00
362	N	0.55	-2.98	0.00
363	Q	0.48	-2.94	0.00
364	A	0.40	-2.97	0.00

		SASA	$\Delta\Delta F$	B-factor
365	F	0.34	-2.98	0.00
366	E	0.26	-2.95	0.00
367	I	0.16	-3.08	0.00
368	S	0.24	-3.18	0.00
369	L	0.32	-3.38	0.00
370	Y	0.36	-3.46	0.00
371	G	0.43	-3.59	0.00
372	T	0.45	-3.52	0.00
373	V	0.54	-3.61	0.00
374	A	0.63	-3.55	0.00
375	E	0.62	-3.56	0.00
376	S	0.71	-3.59	0.00
377	E	0.64	-3.66	0.00
378	N	0.62	-3.80	0.00
379	I	0.59	-3.93	0.00
380	P	0.58	-4.13	0.00
381	F	0.65	-4.38	0.00
382	T	0.54	-4.38	0.00
383	L	0.46	-4.44	0.00
384	P	0.46	-4.39	0.00
385	E	0.44	-4.32	0.00
386	V	0.52	-4.28	0.00
387	S	0.50	-4.30	0.00
388	T	0.53	-4.28	0.00
389	N	0.46	-4.28	0.00
390	K	0.40	-4.32	0.00
391	T	0.42	-4.32	0.00
392	Y	0.42	-4.35	0.00
393	S	0.50	-4.35	0.00
394	F	0.41	-4.39	0.00
395	L	0.44	-4.29	0.00
396	L	0.40	-4.11	0.00
397	Y	0.46	-4.05	0.00
398	T	0.42	-4.03	0.00
399	E	0.44	-4.13	0.00
400	V	0.48	-4.34	0.00
401	D	0.49	-4.59	0.00
402	I	0.47	-4.87	0.00
403	G	0.51	-5.07	0.00
404	E	0.38	-5.33	0.00
405	L	0.40	-5.54	0.00
406	L	0.31	-5.78	0.00

		SASA	$\Delta\Delta F$	B-factor
420	W	1.24	-5.72	82.58
421	S	1.31	-5.56	78.76
422	N	1.12	-5.42	75.42
423	W	1.03	-5.26	71.60
424	W	1.03	-5.06	66.83
425	S	0.83	-4.75	59.43
426	S	0.86	-4.54	54.42
427	P	0.71	-4.36	0.00
428	G	0.47	-4.16	0.00
429	F	0.44	-4.11	0.00
430	D	0.30	-3.83	0.00
431	I	0.44	-3.72	0.00
432	G	0.41	-3.51	0.00
433	K	0.41	-3.50	0.00
434	I	0.43	-3.35	0.00
435	R	0.37	-3.19	0.00
436	V	0.42	-3.06	0.00
437	K	0.48	-3.02	0.00
438	A	0.36	-2.96	0.00
439	G	0.42	-3.04	0.00
440	E	0.36	-3.04	0.00
441	T	0.37	-3.08	0.00
442	Q	0.39	-3.12	0.00
443	K	0.38	-3.22	0.00
444	K	0.41	-3.24	0.00
445	V	0.38	-3.37	0.00
446	I	0.49	-3.43	0.00
447	F	0.63	-3.49	0.00
448	C	0.78	-3.34	0.00
449	S	0.74	-3.36	0.00
450	R	0.74	-3.37	0.00
451	E	0.82	-3.57	31.26
452	K	0.82	-3.72	34.84
453	M	0.85	-3.95	40.33
454	S	0.89	-4.05	42.72
455	Y	0.73	-4.18	0.00
456	L	0.61	-4.22	0.00
457	Q	0.51	-4.19	0.00
458	K	0.50	-4.16	0.00
459	G	0.50	-4.20	0.00
460	K	0.43	-4.21	0.00
461	S	0.43	-4.26	0.00

407	M	0.38	-5.89	0.00
408	L	0.35	-5.92	0.00
409	K	0.34	-5.94	0.00
410	L	0.36	-6.15	0.00
411	K	0.44	-6.31	0.00
412	W	0.46	-6.41	0.00
413	I	0.67	-6.45	0.00
414	S	0.74	-6.33	0.00
415	D	0.76	-6.35	0.00
416	S	0.89	-6.16	93.08
417	Y	0.91	-6.11	91.89
418	F	1.00	-6.01	89.50
419	S	1.23	-5.86	85.92

462	P	0.43	-4.34	0.00
463	V	0.44	-4.44	0.00
464	I	0.49	-4.47	0.00
465	F	0.55	-4.57	0.00
466	V	0.51	-4.48	0.00
467	K	0.58	-4.37	0.00
468	C	0.64	-4.25	0.00
469	H	0.61	-4.09	0.00
470	D	0.74	-4.02	0.00
471	K	0.92	-3.97	40.81
472	S	1.08	-4.14	44.87
473	L	1.13	-4.23	47.02
474	N	1.18	-4.24	47.26

		SASA	$\Delta\Delta F$	B-factor
475	R	1.25	-4.22	46.78
476	K	1.26	-4.18	45.82
477	S	1.35	-3.83	37.47
478	G	1.56	-3.49	29.36

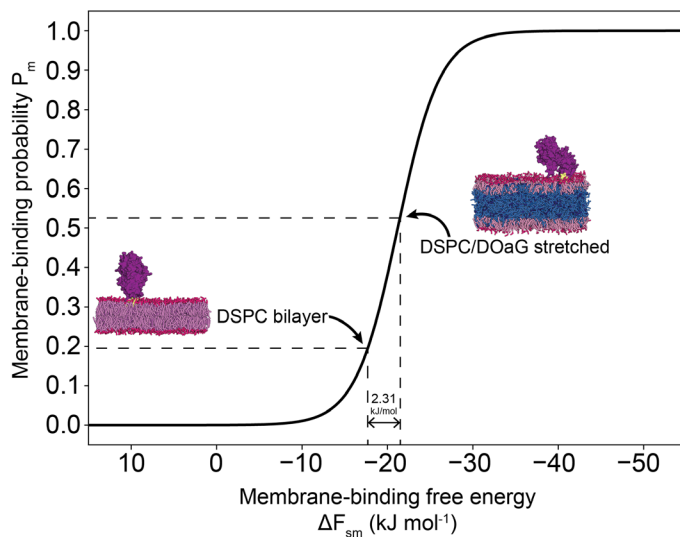


Figure S20. Thermodynamic model describing the relation between membrane-binding free energy ΔF_{sm} and membrane-binding probability P_m , as defined in reference ⁵⁴. When we consider the membrane-binding free energies for bovine LPL to a stretched DSPC/DOaG bilayer and a DSPC bilayer as calculated by umbrella sampling (Fig. 5c in main text), we conclude that a seemingly small free energy difference of 2.31 kJ mol⁻¹, indeed constitutes a large change in membrane-binding probability (dashed lines).

Triacylglycerol lipase	
Superfamily	abH15 - Burkholderia lipases
Homologous family	abH15.02 (Burkholderia cepacia lipase like)
Organism	Burkholderia sp.
Sequences	1
Structures	0
Source DB	
	gi 78063020
Reference Sequence	
	download
MAKTRSRVY AGAVACMSI APFAGTTVAM TLATTHAAMA ASSPADGYTA TRYPIILVHG S SGTDKYAGV LEVWYGIQED	80
LQQNGATVYV ANLSGFQSDD GPNRGEQLL AYYKTVLAAT GATKVIIVGH S GGLSRYV AAVAPDLVAS VTTIGTPHRG	160
SEFADFVQIV LAYDPTGLSS SVTAAFVNVF GILTSSSHNT NQDALAALQT LTTARAATYN QNYPSAGLGA PGSCQTGAPT	240
ETVGGNTHLL YSWAGTAIQP TLSLFGVTGA TDTSTIPVVD PANALDLSTL ALYGTGTMI NRSSGQI S GL VSKCSALYGK	320
VLSTSYKWI S LDEINQLLVG RGAYAEDPVA VIRTHANRLK LAGV	364

Figure S21. Sequence of Triacylglycerol lipase derived from *Burkholderia sp.* Sequence was obtained by the Lipase engineering Database.⁸¹ Sequence does not indicate a Trp-rich domain. BLAST run does not designate significant matches of the protein with any human protein species.

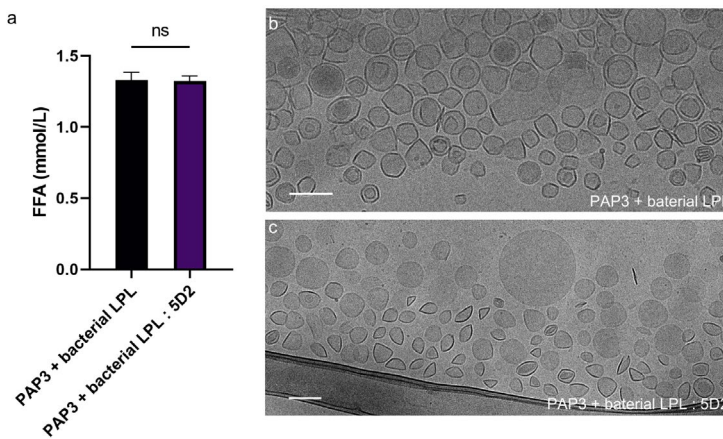


Figure S22. Effect of non-mammalian LPL on PAP3 liposomes with and without 5D2 antibody. **a)** Release of FFA from PAP3 liposomes incubating at 37 °C with non-mammalian LPL (derived from *Burkholderia sp.*) and non-mammalian LPL + 5D2 antibody (1:1) for 120 min. Cryo-TEM images of PAP3 liposomes after incubating at 37 °C for 120 min with **b)** non-mammalian LPL and **c)** non-mammalian LPL + 5D2 antibody (1:1).

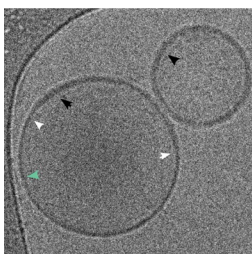


Figure S23. Cryo-TEM image of PAP3 liposomes after incubation with LPL at 37 °C for 180min. Difference of bilayer thickness is indicated with black (thicker part) or green (thinner part) arrows. The point of thickness mismatch is indicated with white arrows.

```

sp|P11150|LIPC_HUMAN
sp|P06858|LIPL_HUMAN
sp|Q9Y5X9|LIPE_HUMAN

MDTSPLCFISILLVLCIFIQSSALGQSLKPEPFGRRAQA-----VETNKTLHEMKTRFLL 54
MESKAL---LVLTLAVWLQSLTAS-RGGV-----AAADQRRDFIDIESKFAL 43
MSN-----SVPLLCFWSLCYCFA-AGSPVPFGEGRLEDKHLHKPKATQTEVKPSPVRFNL 53
*..      : *..: . . .      . : . . : * *
      .

F--GETNQGCQIRINHPDTLQECGFNSSLPLVMI IHGWSVDGVLENWIWQMVAAALKSQP 111
RTPEDTAEDTCHLIPGVAESVATCFHNHSSKTFMVIHGWTVTGMYESWVPKLVAAALYKRE 103
RTSKDPEHEGCYLSVGHSQPLEDCSFNMTAKTFFIIHGWMTSGIFENWLHLKLVSAHRTRE 113
. . : * : . : : * * * : . : * * * : * : * * : : * * * . :
      .

AQPVNVLVDWITLAHDHYTIAVRNTRLVGKEVAALLRWLEESVQLSRSHVHLIGYSLGA 171
-PDSNVIVVDWLSRAQEHYPVSAGYTKLVGQDVARFINWMEEEFNYPDNLVHLLGYSLGA 162
-KDANVVVDWLPALAHQLYTDVAVNTRVVGHSIARMLDWLQEKDDFSLGNVHLIGYSLGA 172
* * : * * : * : * : . * : * * : * : * : * : . : * * * : * * * *
      .

HVSGFAGSSIGGTHKIGRITGLDAAGPLFEGSAPSNRLSPDDANFVDAIHTFTREHMGLS 231
HAAGIAGSLTNK--KVNRI TGLDPAGPNFEYAEAPSRLSPDDADFDVLHFTTRGSPGRS 220
HVAGYAGNFVKG--TVGRITGLDPAGPMFEGADIHKRLSPDDADFDVLHFTYTRS-FGLS 229
* : * * * . . : * * * * * * * * * : . * * * * * * * * * : * * * * * *
      .

VGIKQPIGHYDFYPNGGSFQPGCHFLELYRHIAQHGFNAITQTIKCSHERSVHLFIDSL 291
IGIQKPVGHVDIYPNGGTQPGCNIGEAIRVIAERGLGDVDQLVKCSHERSIHLFIDSL 280
IGIQMPVGHIDIYPNGGDFQPGCGLNDVLGSI--AYGTITEVVKCEHERAVHLFVDSL 286
: * * : * * * * * * * * * * : : * . . : : * * * * * * * * * *
      .

HAGTQSMAYPCGDMNSFSQGLCLSCCKGRCNTLGYHVRQEPKRSKSKRLFLVTRAQSPFKV 351
NEENPSKAYRCSKAEFEKGLCLSCRKNRCNNGYEINKVRAKRSKMYLKTQRSQMPYKV 340
NQDKPSFAFQCTDSNRFKKGI CLSCRKNRCNSIGYNAKMRNKRNSKMYLKTTRAGMPFRV 346
: . * * : * . : * . : * * * * * * * * * . : . . . . : * * * : * * *
      .

YHYQFKIQFINQ-TETPIQTFTFMSLLGTKEKMQKIPITLGKGIASNKTYSFLLITLDVDI 410
FHYQVKIHFSGTESEHTNQAFEISLYGTVAESENIPFTLPE-VSTNKTYSFLLIYTEVDI 399
YHYQMKIHVFSYKNMGEIEPTFYVTLYGTNADSQTLPLEIVERIEQNATNTFLVYTEEDL 406
: * * * * * . . . : * : * * * . . : * : : : * * * * * : * *
      .

GELIMIKFKWENSA--VWANVVDIVQTIIPWSTGPRHSGVLVLTIRVKAGETQQRMTFCS 468
GELLMLKLLKWKSDSYF--SWSDWWS-----PGFAIQKIRVKAGETQKKVIFCS 446
GDLLKIQLTWEGASQ--SWYNLWKEFRSYLSQPRNP-GRELNIRIRVKSGETQKLTFTCT 464
* : * : : * * . : * : * . : : * * * * * * * * * : * *
      .

ENTDLLLLRPTQEKIFVKCEIKSKTSKRKIR----- 499
REKVSHLQKGKAPAVFVKCHDKSLNKKSG----- 475
EDPENTSI SPGRELWFRKCRDGWRMKNETSPTVELP 500
. : . * * * . :

```

Figure S24. Sequence alignment of Triacylglycerol Lipases Hepatic, Lipoprotein and Endothelial Lipase (*Homo Sapiens*). Sequence alignment was run by an alignment tool provided by Uniprot.org database. Uniprot IDs: P11150 (in magenta), P06858 (in blue) and Q9Y5X9 (in black) respectively. Conserved amino acids indicated with *. Similar amino acids indicated with “:”, somewhat similar amino acids indicated with “.”. Tryptophan-rich loop indicated in purple box.

```

sp|P11151|LIPL_BOVIN
sp|P06858|LIPL_HUMAN

MESKALLLLALSVCQLQSLTIVSRGGLVAADRITGGKDFRDIESKFALRTPEDTAEDTCHLI 60
MESKALLVLTAVWLQSLTASRGGVAAADQ--RRDFIDIESKFALRTPEDTAEDTCHLI 57
*****:*:*:* *****:***:.**: :** *****

PGVTESVANCHFNHSSKTFVVIHGWTVTGMYESWVVKLVAAALYKREPDSNVIVVDWLSRA 120
PGVAESVATCHFNHSSKTFMVIHGWTVTGMYESWVVKLVAAALYKREPDSNVIVVDWLSRA 117
**:*:**.******:*****

QQHYPVSAAGYTKLVGQDVAKFNMWMADEFNYPLGNVHLLGYSLGAAHAAGIAGSLTNKKVN 180
QEHYPVSAAGYTKLVGQDVARFINWMEEEFNYPDLDNVHLLGYSLGAAHAAGIAGSLTNKKVN 177
*:******:.*** :*****.******

RITGLDPAGPNFEYAEAPSRLSPDDADFVDVLHFTFRGSPGRSIGIQKPVGHVDIYPNGG 240
RITGLDPAGPNFEYAEAPSRLSPDDADFVDVLHFTFRGSPGRSIGIQKPVGHVDIYPNGG 237
*****

TFQPGCNIGEALRVIAERGLGDVDQLVKCSHERSVHLFIDSLNNEENPSKAYRCSKEAF 300
TFQPGCNIGEALRVIAERGLGDVDQLVKCSHERSIHLFIDSLNNEENPSKAYRCSKEAF 297
*****:*****.******.***

EKGLCLSCRNRCNNMGYEINKVRAKRSSKMYLKTRSQMPYKVFHYQVKIHFSGTESNTY 360
EKGLCLSCRNRCNNLGYEINKVRAKRSSKMYLKTRSQMPYKVFHYQVKIHFSGTESETH 357
*****.******:.*

TNQAFEISLYGTVAESENIPFTLPEVSTNKTYSFLLYTEVDIGELLMLKWKWISDSYFSW 420
TNQAFEISLYGTVAESENIPFTLPEVSTNKTYSFLLYTEVDIGELLMLKWKWISDSYFSW 417
*****.******.***

SNWWSSEGFDIGKIRVKAGETQKKVIFCSREKMSYLQKGSFVIFVKCHDKSLNRKSG 478
SDWWSSEGFVAIQKIRVKAGETQKKVIFCSREKMSYHLQKGPAPVVFVKCHDKSLNRKSG 475
*:******.******:.******:.*:*****

```

Figure S25. Sequence alignment of LPL derived from *Bos Taurus* (bovine) and *Homo Sapiens* (Human). Sequence alignment was run by an alignment tool provided by Uniprot.org database showing 92.21% homology. Uniprot IDs: P11151 for Bovine LPL (in blue) and P06858 for Human LPL (in black). Conserved amino acids indicated with *. Similar amino acids indicated with “:”, somewhat similar amino acids indicated with “.”. Tryptophan-rich loop indicated in purple box.

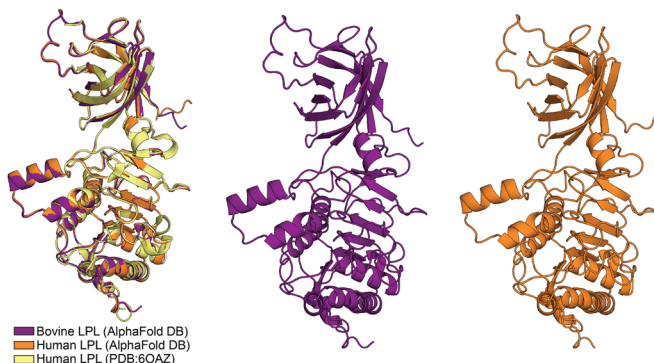


Figure S26. AlphaFold and X-ray protein structures overlap. The AlphaFold DB ^{72,73} models of bovine and human LPL closely overlap with the human LPL crystal structure (PDB: 6OAZ).⁵¹

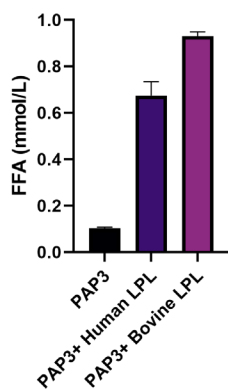


Figure S27. Release of FFA from PAP3 liposomes incubating with Human LPL and Bovine LPL. PAP3 liposomes incubating at 37 °C with LPL for 120 min.

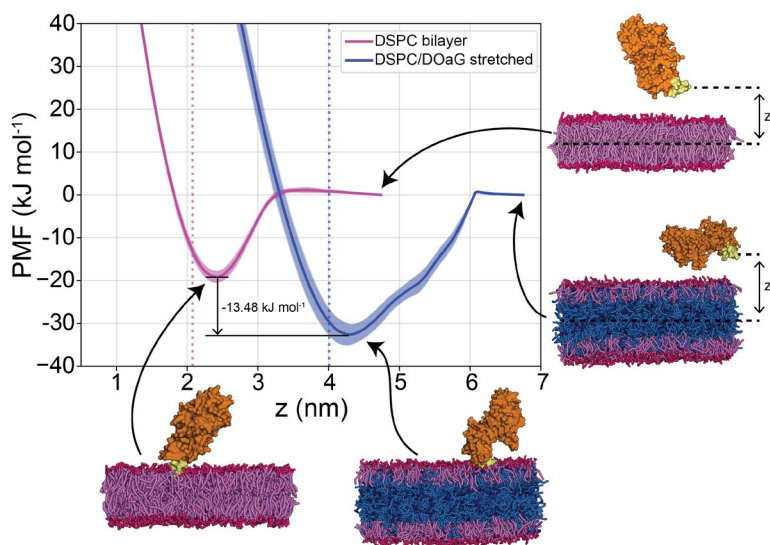


Figure S28. Potential of mean force (PMF) profiles of human LPL binding to a DSPC bilayer (in red-pink) and a DSPC/DOaG phase-separated membrane (in red-pink/blue). The US reaction coordinate is the z-distance between the COM of the Trp-rich loop (in yellow) and the COM of the lipids (i.e., center plane of the membrane). Snapshots are the final frames of the trajectories and indicate that the protein is completely unbound at high z (free energy = 0 kJ mol⁻¹) and membrane-bound through the Trp-rich loop at the minima. Dotted lines indicate the position of the DSPC head groups (NC3 beads).

Table S1. Physicochemical properties of liposomes

Formulation	Size (nm)	PDI	T (°C)	Formulation	Size (nm)	PDI	T (°C)
PAP3	± 143.2	0.294	25	PAP3 + LPL:XEN445 0 µM	±147.5	0.124	37
PAP3 30 min	± 151.8	0.330	37	PAP3 + LPL:XEN445 50 µM	±146.9	0.117	37
PAP3 120 min	± 154.4	0.370	37	PAP3 + LPL:XEN445 100 µM	±147.4	0.110	37
PAP3 300 min	± 150.8	0.350	37	PAP3 + LPL:XEN445 500 µM	±141.2	0.116	37
PAP3 + LPL 30 min	± 159.5	0.085	37	PAP3 + LPL:XEN445 1000 µM	±136.7	0.099	37
PAP3 + LPL 120 min	± 158.5	0.104	37	PAP3 (10% DOaG)	±97.5	0.051	25
PAP3 + LPL 300 min	± 166.0	0.200	37	PAP3 (20% DOaG)	±139.3	0.230	25
PAP3 + inactive LPL 30 min	± 146.3	0.275	37	PAP3 (30% DOaG)	±109.3	0.140	25
PAP3 + inactive LPL 120 min	± 141.5	0.256	37	PAP3 (10% DOaG) + LPL	±106.5	0.072	37
PAP3 + inactive LPL 300 min	± 140.4	0.269	37	PAP3 (20% DOaG) + LPL	±104.5	0.047	37
DSPC	± 135.7	0.344	37	PAP3 (30% DOaG) + LPL	±115.3	0.103	37
DSPC + LPL 30 min	± 142.0	0.265	37	PAP3 + LPL:5D2	±151.8	0.184	37
DSPC + LPL 120 min	± 148.4	0.382	37	PAP3 + LPL:IgG	±158.7	0.182	37
DSPC + LPL 300 min	± 128.1	0.208	37	PAP3 + bacterial LPL	±155.0	0.156	37
Myocet®-like (POPC:CHO_55:45) + LPL	± 114.2	0.065	37	PAP3 + bacterial LPL:5D2	±149.4	0.143	37

3.6 References

1. Bulbake, U.; Doppalapudi, S.; Kommineni, N.; Khan, W. Liposomal Formulations in Clinical Use: An Updated Review. *Pharmaceutics* **2017**, *9* (2), 12.
2. Cullis, P. R.; Hope, M. J. Lipid Nanoparticle Systems for Enabling Gene Therapies. *Mol Ther* **2017**, *25* (7), 1467–1475.
3. Akinc, A.; Maier, M. A.; Manoharan, M.; Fitzgerald, K.; Jayaraman, M.; Barros, S.; Ansell, S.; Du, X.; Hope, M. J.; Madden, T. D.; Mui, B. L.; Semple, S. C.; Tam, Y. K.; Ciufolini, M.; Witzigmann, D.; Kulkarni, J. A.; van der Meel, R.; Cullis, P. R. The Onpattro Story and the Clinical Translation of Nanomedicines Containing Nucleic Acid-Based Drugs. *Nat Nanotechnol* **2019**, *14* (12), 1084–1087.
4. Kulkarni, J. A.; Darjuan, M. M.; Mercer, J. E.; Chen, S.; van der Meel, R.; Thewalt, J. L.; Yi Tam, Y. C.; Cullis, P. R. On the Formation and Morphology of Lipid Nanoparticles Containing Ionizable Cationic Lipids and siRNA. *ACS Nano* **2018**, *12* (5), 4787–4795.
5. Schoenmaker, L.; Witzigmann, D.; Kulkarni, J. A.; Verbeke, R.; Kersten, G.; Jiskoot, W.; Crommelin, D. J. A. mRNA-Lipid Nanoparticle COVID-19 Vaccines: Structure and Stability. *Int J Pharm* **2021**, *601*, 120586.
6. Hou, X.; Zaks, T.; Langer, R.; Dong, Y. Lipid Nanoparticles for mRNA Delivery. *Nat Rev Mat* **2021**, *6* (12), 1078–1094.
7. Francia, V.; Schifflers, R. M.; Cullis, P. R.; Witzigmann, D. The Biomolecular Corona of Lipid Nanoparticles for Gene Therapy. *Bioconjug Chem* **2020**, *31* (9), 2046–2059.
8. Pattipeiluhu, R.; Crielaard, S.; Klein-Schiphorst, I.; Florea, B. I.; Kros, A.; Campbell, F. Unbiased Identification of the Liposome Protein Corona Using Photoaffinity-Based Chemoproteomics. *ACS Cent Sci* **2020**, *6* (4), 535–545.
9. Hadjidemetriou, M.; Mcadam, S.; Garner, G.; Thackeray, C.; Knight, D.; Smith, D.; Al-Ahmady, Z.; Mazza, M.; Rogan, J.; Clamp, A.; Kostarelos, K.; Hadjidemetriou, M.; Al-Ahmady, Z.; Mazza, M.; Kostarelos, K.; Mcadam, S.; Garner, G.; Rogan, J.; Thackeray, C.; Clamp, A.; Knight, D.; Smith, D. The Human in vivo Biomolecule Corona onto PEGylated Liposomes: A Proof-of-Concept Clinical Study. *Adv Mater* **2019**, *31* (4), 1803335.
10. Hadjidemetriou, M.; Kostarelos, K. Evolution of the Nanoparticle Corona. *Nat Nanotechnol* **2017**, *12* (4), 288–290.
11. Holme, M. N.; Rashid, M. H.; Thomas, M. R.; Barriga, H. M. G.; Herpoldt, K. L.; Heenan, R. K.; Dreiss, C. A.; Bañuelos, J. L.; Xie, H. N.; Yarovsky, I.; Stevens, M. M.

- Fate of Liposomes in the Presence of Phospholipase C and D: From Atomic to Supramolecular Lipid Arrangement. *ACS Cent Sci* **2018**, *4* (8), 1023–1030.
12. Fong, W. K.; Sánchez-Ferrer, A.; Rappolt, M.; Boyd, B. J.; Mezzenga, R. Structural Transformation in Vesicles upon Hydrolysis of Phosphatidylethanolamine and Phosphatidylcholine with Phospholipase C. *Langmuir* **2019**, *35* (46), 14949–14958.
 13. Arias-Alpizar, G.; Papadopoulou, P.; Rios, X.; Pulagam, K. R.; Moradi, M. A.; Pattipeiluhu, R.; Bussmann, J.; Sommerdijk, N.; Llop, J.; Kros, A.; Campbell, F. Phase-Separated Liposomes Hijack Endogenous Lipoprotein Transport and Metabolism Pathways to Target Subsets of Endothelial Cells in vivo. *Adv Healthc Mater* **2023**, *12* (10), e2202709.
 14. Bolen, E. J.; Sando, J. J. Effect of Phospholipid Unsaturation on Protein Kinase C Activation. *Biochemistry* **1992**, *31* (25), 5945–5951.
 15. Goñi, F. M.; Alonso, A. Structure and Functional Properties of Diacylglycerols in Membranes. *Prog Lipid Res* **1999**, *38* (1), 1–48.
 16. Goldberg, E. M.; Lester, D. S.; Borchardt, D. B.; Zidovetzki, R. Effects of Diacylglycerols on Conformation of Phosphatidylcholine Headgroups in Phosphatidylcholine/Phosphatidylserine Bilayers. *Biophys J* **1995**, *69* (3), 965–973.
 17. Campomanes, P.; Zoni, V.; Vanni, S. Local Accumulation of Diacylglycerol Alters Membrane Properties Nonlinearly Due to Its Transbilayer Activity. *Commun Chem* **2019**, *2* (1), 1–8.
 18. Alwarawrah, M.; Hussain, F.; Huang, J. Alteration of Lipid Membrane Structure and Dynamics by Diacylglycerols with Unsaturated Chains. *Biochim Biophys Acta Biomembr* **2016**, *1858* (2), 253–263.
 19. Vanni, S.; Hirose, H.; Barelli, H.; Antonny, B.; Gautier, R. A Sub-Nanometre View of How Membrane Curvature and Composition Modulate Lipid Packing and Protein Recruitment. *Nat Commun* **2014**, *5* (1), 1–10.
 20. Alwarawrah, M.; Dai, J.; Huang, J. Modification of Lipid Bilayer Structure by Diacylglycerol: A Comparative Study of Diacylglycerol and Cholesterol. *J Chem Theory Comput* **2012**, *8* (2), 749–758.
 21. Goldberg, E. M.; Lester, D. S.; Borchardt, D. B.; Zidovetzki, R. Effects of Diacylglycerols and Ca²⁺ on Structure of Phosphatidylcholine/Phosphatidylserine Bilayers. *Biophys J* **1994**, *66*, 382–393.
 22. Vamparys, L.; Gautier, R.; Vanni, S.; Bennett, W. F. D.; Tieleman, D. P.; Antonny, B.; Etchebest, C.; Fuchs, P. F. J. Conical Lipids in Flat Bilayers Induce Packing Defects Similar to That Induced by Positive Curvature. *Biophys J* **2013**, *104* (3), 585–593.

23. Drin, G.; Casella, J.-F.; Gautier, R.; Boehmer, T.; Schwartz, T. U.; Antonny, B. A General Amphipathic A-Helical Motif for Sensing Membrane Curvature. *Nat Struct Mol Biol* **2007**, *14* (2), 138–146.
24. Hatzakis, N. S.; Bhatia, V. K.; Larsen, J.; Madsen, K. L.; Bolinger, P. Y.; Kunding, A. H.; Castillo, J.; Gether, U.; Hedegård, P.; Stamou, D. How Curved Membranes Recruit Amphipathic Helices and Protein Anchoring Motifs. *Nat Chem Biol* **2009**, *5* (11), 835–841.
25. Vanni, S.; Vamparys, L.; Gautier, R.; Drin, G.; Etchebest, C.; Fuchs, P. F. J.; Antonny, B. Amphipathic Lipid Packing Sensor Motifs: Probing Bilayer Defects with Hydrophobic Residues. *Biophys J* **2013**, *104* (3), 575–584.
26. Wildermuth, K. D.; Monje-Galvan, V.; Warburton, L. M.; Klauda, J. B. Effect of Membrane Lipid Packing on Stable Binding of the ALPS Peptide. *J Chem Theory Comput* **2019**, *15* (2), 1418–1429.
27. Kim, S.; Oh, M. I.; Swanson, J. M. J. Stressed Lipid Droplets: How Neutral Lipids Relieve Surface Tension and Membrane Expansion Drives Protein Association. *J Phys Chem B* **2021**, *125* (21), 5572–5586.
28. Barlič, A.; Gutiérrez-Aguirre, I.; Caaveiro, J. M. M.; Cruz, A.; Ruiz-Argüello, M. B.; Pérez-Gil, J.; González-Mañas, J. M. Lipid Phase Coexistence Favors Membrane Insertion of Equinatoxin-II, a Pore-Forming Toxin from Actinia Equina. *J Biol Chem* **2004**, *279* (33), 34209–34216.
29. Ahyauch, H.; Sot, J.; Collado, M. I.; Huarte, N.; Requejo-Isidro, J.; Alonso, A.; Goñi, F. M. End-Product Diacylglycerol Enhances the Activity of PI-PLC through Changes in Membrane Domain Structure. *Biophys J* **2015**, *108* (7), 1672–1682.
30. Bohr, S. S. R.; Thorlaksen, C.; Kühnel, R. M.; Günther-Pomorski, T.; Hatzakis, N. S. Label-Free Fluorescence Quantification of Hydrolytic Enzyme Activity on Native Substrates Reveals How Lipase Function Depends on Membrane Curvature. *Langmuir* **2020**, *36* (23), 6473–6481.
31. Fuki, I. V.; Blanchard, N.; Jin, W.; Marchadier, D. H. L.; Millar, J. S.; Glick, J. M.; Rader, D. J. Endogenously Produced Endothelial Lipase Enhances Binding and Cellular Processing of Plasma Lipoproteins via Heparan Sulfate Proteoglycan-Mediated Pathway. *J Biol Chem* **2003**, *278* (36), 34331–34338.
32. Merkel, M.; Kako, Y.; Radner, H.; Cho, I. S.; Ramasamy, R.; Brunzell, J. D.; Goldberg, I. J.; Breslow, J. L. Catalytically Inactive Lipoprotein Lipase Expression in Muscle of Transgenic Mice Increases Very Low Density Lipoprotein Uptake: Direct Evidence That Lipoprotein Lipase Bridging Occurs in vivo. *PNAS* **1998**, *95* (23), 13841–13846.

33. Connelly, P. W. The Role of Hepatic Lipase in Lipoprotein Metabolism. *Clin Chim Acta* **1999**, 286 (1–2), 243–255.
34. Mead, J. R.; Irvine, S. A.; Ramji, D. P. Lipoprotein Lipase: Structure, Function, Regulation, and Role in Disease. *J Mol Med* **2002**, 80 (12), 753–769.
35. Jaye, M.; Lynch, K. J.; Krawiec, J.; Marchadier, D.; Maugeais, C.; Doan, K.; South, V.; Amin, D.; Perrone, M.; Rader, D. J. A Novel Endothelial-Derived Lipase That Modulates HDL Metabolism. *Nat Genet* **1999**, 21 (4), 424–428.
36. Wang, Z.; Li, S.; Sun, L.; Fan, J.; Liu, Z. Comparative Analyses of Lipoprotein Lipase, Hepatic Lipase, and Endothelial Lipase, and Their Binding Properties with Known Inhibitors. *PLOS One* **2013**, 8 (8), 72146.
37. Choi, S. Y.; Hirata, K.; Ishida, T.; Quertermous, T.; Cooper, A. D. Endothelial Lipase. *J Lipid Res* **2002**, 43 (11), 1763–1769.
38. Lookene, A.; Groot, N. B.; Kastelein, J. J. P.; Olivecrona, G.; Bruin, T. Mutation of Tryptophan Residues in Lipoprotein Lipase. Effects on Stability, Immunoreactivity, and Catalytic Properties. *J Biol Chem* **1997**, 272 (2), 766–772.
39. Williams, S. E.; Inoue, I.; Tran, H.; Fry, G. L.; Pladet, M. W.; Iverius, P. H.; Lalouel, J. M.; Chappell, D. A.; Strickland, D. K. The Carboxyl-Terminal Domain of Lipoprotein Lipase Binds to the Low Density Lipoprotein Receptor-Related Protein/Alpha 2-Macroglobulin Receptor (LRP) and Mediates Binding of Normal Very Low Density Lipoproteins to LRP. *J Biol Chem* **1994**, 269 (12), 8653–8658.
40. Goulbourne, C. N.; Gin, P.; Tatar, A.; Nobumori, C.; Hoenger, A.; Jiang, H.; Grovenor, C. R. M.; Adeyo, O.; Esko, J. D.; Goldberg, I. J.; Reue, K.; Tontonoz, P.; Bensadoun, A.; Beigneux, A. P.; Young, S. G.; Fong, L. G. The GPIHBP1-LPL Complex Is Responsible for the Margination of Triglyceride-Rich Lipoproteins in Capillaries. *Cell Metab* **2014**, 19 (5), 849–860.
41. Yu, J. E.; Han, S. Y.; Wolfson, B.; Zhou, Q. The Role of Endothelial Lipase in Lipid Metabolism, Inflammation, and Cancer. *Histol Histopathol* **2018**, 33 (1), 1–10.
42. Borén, J.; Lookene, A.; Makoveichuk, E.; Xiang, S.; Gustafsson, M.; Liu, H.; Talmud, P.; Olivecrona, G. Binding of Low Density Lipoproteins to Lipoprotein Lipase Is Dependent on Lipids but Not on Apolipoprotein B. *J Biol Chem* **2001**, 276 (29), 26916–26922.
43. De Man, F. H. A. F.; De Beer, F.; Van Der Laarse, A.; Smelt, A. H. M.; Havekes, L. M. Lipolysis of Very Low Density Lipoproteins by Heparan Sulfate Proteoglycan-Bound Lipoprotein Lipase. *J Lipid Res* **1997**, 38 (12), 2465–2472.

44. Perdomo, G.; Kim, D. H.; Zhang, T.; Qu, S.; Thomas, E. A.; Toledo, F. G. S.; Slusher, S.; Fan, Y.; Kelley, D. E.; Dong, H. H. A Role of Apolipoprotein D in Triglyceride Metabolism. *J Lipid Res* **2010**, *51* (6), 1298–1311.
45. Batist, G.; Barton, J.; Chaikin, P.; Swenson, C.; Welles, L. Myocet (Liposome-Encapsulated Doxorubicin Citrate): A New Approach in Breast Cancer Therapy. *Expert Opin Pharmacother* **2002**, *3* (12), 1739–1751.
46. Sun, S.; Dean, R.; Jia, Q.; Zenova, A.; Zhong, J.; Grayson, C.; Xie, C.; Lindgren, A.; Samra, P.; Sojo, L.; Van Heek, M.; Lin, L.; Percival, D.; Fu, J. M.; Winther, M. D.; Zhang, Z. Discovery of XEN445: A Potent and Selective Endothelial Lipase Inhibitor Raises Plasma HDL-Cholesterol Concentration in Mice. *Bioorg Med Chem* **2013**, *21* (24), 7724–7734.
47. Rigoni, M.; Caccin, P.; Gschmeissner, S.; Koster, G.; Postle, A. D.; Rossetto, O.; Schiavo, G.; Montecucco, C. Neuroscience: Equivalent Effects of Snake PLA2 Neurotoxins and Lysophospholipid - Fatty Acid Mixtures. *Science* **2005**, *310* (5754), 1678–1680.
48. Souza, P. C. T.; Alessandri, R.; Barnoud, J.; Thallmair, S.; Faustino, I.; Grünwald, F.; Patmanidis, I.; Abdizadeh, H.; Bruininks, B. M. H.; Wassenaar, T. A.; Kroon, P. C.; Melcr, J.; Nieto, V.; Corradi, V.; Khan, H. M.; Domański, J.; Javanainen, M.; Martinez-Seara, H.; Reuter, N.; Best, R. B.; Vattulainen, I.; Monticelli, L.; Periolo, X.; Tieleman, D. P.; de Vries, A. H.; Marrink, S. J. Martini 3: A General Purpose Force Field for Coarse-Grained Molecular Dynamics. *Nat Methods* **2021**, *18* (4), 382–388.
49. Liu, Y.; de Vries, A. H.; Pezeshkian, W.; Marrink, S. J. Capturing Membrane Phase Separation by Dual Resolution Molecular Dynamics Simulations. *J Chem Theory Comput* **2021**, *17* (9), 5876–5884.
50. Van Hilten, N.; Stroh, K. S.; Risselada, H. J. Efficient Quantification of Lipid Packing Defect Sensing by Amphipathic Peptides: Comparing Martini 2 and 3 with CHARMM36. *J Chem Theory Comput* **2022**, *18* (7), 4503–4514.
51. Arora, R.; Nimonkar, A. V.; Baird, D.; Wang, C.; Chiu, C. H.; Horton, P. A.; Hanrahan, S.; Cubbon, R.; Weldon, S.; Tschantz, W. R.; Mueller, S.; Brunner, R.; Lehr, P.; Meier, P.; Ottl, J.; Voznesensky, A.; Pandey, P.; Smith, T. M.; Stojanovic, A.; Flyer, A.; Benson, T. E.; Romanowski, M. J.; Trauger, J. W. Structure of Lipoprotein Lipase in Complex with GPIHBP1. *PNAS* **2019**, *116* (21), 10360–10365.
52. Gunn, K. H.; Roberts, B. S.; Wang, F.; Strauss, J. D.; Borgnia, M. J.; Egelman, E. H.; Neher, S. B. The Structure of Helical Lipoprotein Lipase Reveals an Unexpected Twist in Lipase Storage. *PNAS* **2020**, *117* (19), 10254–10264.

53. Wong, H.; Davis, R. C.; Thuren, T.; Goers, J. W.; Nikazy, J.; Waite, M.; Schotz, M. C. Lipoprotein Lipase Domain Function. *J Biol Chem* **1994**, *269* (14), 10319–10323.
54. van Hilten, N.; Methorst, J.; Verwei, N.; Risselada, H. J. Physics-Based Generative Model of Curvature Sensing Peptides; Distinguishing Sensors from Binders. *Sci Adv* **2023**, *9* (11), eade8839.
55. Cui, H.; Lyman, E.; Voth, G. A. Mechanism of Membrane Curvature Sensing by Amphipathic Helix Containing Proteins. *Biophys J* **2011**, *100* (5), 1271–1279.
56. Santamarina-Fojo, S.; Dugi, K. A. Structure, Function and Role of Lipoprotein Lipase in Lipoprotein Metabolism. *Curr Opin Lipidol* **1994**, *5* (2), 117–125.
57. Prévost, C.; Sharp, M. E.; Kory, N.; Lin, Q.; Voth, G. A.; Farese, R. V.; Walther, T. C. Mechanism and Determinants of Amphipathic Helix-Containing Protein Targeting to Lipid Droplets. *Dev Cell* **2018**, *44* (1), 73–86.e4.
58. Kim, S.; Swanson, J. M. J.; Voth, G. A. Computational Studies of Lipid Droplets. *J Phys Chem B* **2022**, *126* (11), 2145–2154.
59. Luz, J. G.; Beigneux, A. P.; Asamoto, D. A. K.; He, C.; Song, W.; Allan, C. M.; Morales, J.; Tu, Y.; Kwok, A.; Cottle, T.; Meiyappan, M.; Fong, L. G.; Kim, J. E.; Ploug, M.; Young, S. G.; Birrane, G. The Structural Basis for Monoclonal Antibody 5D2 Binding to the Tryptophan-Rich Loop of Lipoprotein Lipase. *J Lipid Res* **2020**, *61* (10), 1347–1359.
60. Chang, S. F.; Reich, B.; Brunzell, J. D.; Will, H. Detailed Characterization of the Binding Site of the Lipoprotein Lipase-Specific Monoclonal Antibody 5D2. *J Lipid Res* **1998**, *39* (12), 2350–2359.
61. Kristensen, K. K.; Leth-Espensen, K. Z.; Mertens, H. D. T.; Birrane, G.; Meiyappan, M.; Olivecrona, G.; Jørgensen, T. J. D.; Young, S. G.; Ploug, M. Unfolding of Monomeric Lipoprotein Lipase by ANGPTL4: Insight into the Regulation of Plasma Triglyceride Metabolism. *PNAS* **2020**, *117* (8), 4337–4346.
62. Wu, S. A.; Kersten, S.; Qi, L. Lipoprotein Lipase and Its Regulators: An Unfolding Story. *Trends Endocrinol Metab* **2021**, *32* (1), 48–61.
63. Kersten, S. Physiological Regulation of Lipoprotein Lipase. *Biochim Biophys Acta* **2014**, *1841* (7), 919–933.
64. Cornell, C. E.; Mileant, A.; Thakkar, N.; Lee, K. K.; Keller, S. L. Direct Imaging of Liquid Domains in Membranes by Cryo-Electron Tomography. *PNAS* **2020**, *117* (33), 19713–19719.
65. Heberle, F. A.; Doktorova, M.; Scott, H. L.; Skinkle, A. D.; Waxham, M. N.; Levental, I. Direct Label-Free Imaging of Nanodomains in Biomimetic and Biological Membranes by Cryogenic Electron Microscopy. *PNAS* **2020**, *117* (33), 19943–19952.

66. Khetarpal, S. A.; Vitali, C.; Levin, M. G.; Klarin, D.; Park, J.; Pampana, A.; Millar, J. S.; Kuwano, T.; Sugasini, D.; Subbaiah, P. V.; Billheimer, J. T.; Natarajan, P.; Rader, D. J. Endothelial Lipase Mediates Efficient Lipolysis of Triglyceride-Rich Lipoproteins. *PLoS Genet* **2021**, *17* (9), e1009802.
67. Olivecrona, G.; Olivecrona, T. Triglyceride Lipases and Atherosclerosis. *Curr Opin Lipidol* **2010**, *21* (5), 409–415.
68. Watt, M. J.; Spriet, L. L. Triacylglycerol Lipases and Metabolic Control: Implications for Health and Disease. *Am J Physiol Endocrinol Metab* **2010**, *299* (2), 162–168.
69. Abraham, M. J.; Murtola, T.; Schulz, R.; Páll, S.; Smith, J. C.; Hess, B.; Lindahl, E. GROMACS: High Performance Molecular Simulations through Multi-Level Parallelism from Laptops to Supercomputers. *SoftX* **2015**, *1*, 19–25.
70. Martinez, L.; Andrade, R.; Birgin, E. G.; Martínez, J. M. PACKMOL: A Package for Building Initial Configurations for Molecular Dynamics Simulations. *J Comput Chem* **2009**, *30* (13), 2157–2164.
71. Gautier, R.; Bacle, A.; Tiberti, M. L.; Fuchs, P. F.; Vanni, S.; Antonny, B. PackMem: A Versatile Tool to Compute and Visualize Interfacial Packing Defects in Lipid Bilayers. *Biophys J* **2018**, *115* (3), 436–444.
72. Jumper, J.; Evans, R.; Pritzel, A.; Green, T.; Figurnov, M.; Ronneberger, O.; Tunyasuvunakool, K.; Bates, R.; Židek, A.; Potapenko, A.; Bridgland, A.; Meyer, C.; Kohl, S. A. A.; Ballard, A. J.; Cowie, A.; Romera-Paredes, B.; Nikolov, S.; Jain, R.; Adler, J.; Back, T.; Petersen, S.; Reiman, D.; Clancy, E.; Zielinski, M.; Steinegger, M.; Pacholska, M.; Berghammer, T.; Bodenstein, S.; Silver, D.; Vinyals, O.; Senior, A. W.; Kavukcuoglu, K.; Kohli, P.; Hassabis, D. Highly Accurate Protein Structure Prediction with AlphaFold. *Nature* **2021**, *596* (7873), 583–589.
73. Varadi, M.; Anyango, S.; Deshpande, M.; Nair, S.; Natassia, C.; Yordanova, G.; Yuan, D.; Stroe, O.; Wood, G.; Laydon, A.; Židek, A.; Green, T.; Tunyasuvunakool, K.; Petersen, S.; Jumper, J.; Clancy, E.; Green, R.; Vora, A.; Lutfi, M.; Figurnov, M.; Cowie, A.; Hobbs, N.; Kohli, P.; Kleywegt, G.; Birney, E.; Hassabis, D.; Velankar, S. AlphaFold Protein Structure Database: Massively Expanding the Structural Coverage of Protein-Sequence Space with High-Accuracy Models. *Nucleic Acids Res* **2022**, *50* (D1), D439–D444.
74. Cock, P. J. A.; Antao, T.; Chang, J. T.; Chapman, B. A.; Cox, C. J.; Dalke, A.; Friedberg, I.; Hamelryck, T.; Kauff, F.; Wilczynski, B.; De Hoon, M. J. L. Biopython: Freely Available Python Tools for Computational Molecular Biology and Bioinformatics. *Bioinformatics* **2009**, *25* (11), 1422–1423.

75. Wassenaar, T. A.; Ingólfsson, H. I.; Böckmann, R. A.; Tieleman, D. P.; Marrink, S. J. Computational Lipidomics with Insane: A Versatile Tool for Generating Custom Membranes for Molecular Simulations. *J Chem Theory Comput* **2015**, *11* (5), 2144–2155.
76. Cornelis Kroon, P. Aggregate Assemble Automate. **2020**.
77. Kabsch, W.; Sander, C. Dictionary of Protein Secondary Structure: Pattern Recognition of Hydrogen-Bonded and Geometrical Features. *Biopolymers* **1983**, *22* (12), 2577–2637.
78. Kästner, J.; Thiel, W. Bridging the Gap between Thermodynamic Integration and Umbrella Sampling Provides a Novel Analysis Method: “Umbrella Integration.” *J Chem Phys* **2005**, *123* (14), 144104.
79. Bligh, E. G.; Dyer, W. J. A Rapid Method of Total Lipid Extraction and Purification. *Can J Biochem Physiol* **1959**, *37* (8), 911–917.
80. Liu, Y.; de Vries, A. H.; Pezeshkian, W.; Marrink, S. J. Capturing Membrane Phase Separation by Dual Resolution Molecular Dynamics Simulations. *J Chem Theory Comput* **2021**, *17* (9), 5876–5884.
81. Fischer, M.; Pleiss, J. The Lipase Engineering Database: A Navigation and Analysis Tool for Protein Families. *Nucleic Acids Res* **2003**, *31* (1), 319–321.